Check for updates

Halide perovskite-based nanomaterials for the detection and photocatalytic removal of gaseous pollutants

Zhijian Xiao,[a] Jialin Li,[a] Xueyi Mai,[b] Jingling Yang*[a] and Mingshan Zhu 🆔 *[a]

Halide perovskite-based nanomaterials have attracted considerable attention in the field of detection and photocatalytic removal of gaseous pollutants. These nanomaterials not only exhibit a strong response to visible light and good photocatalytic activity but also demonstrate high sensitivity and selectivity in the detection of gaseous pollutants. Consequently, they are expected to play a significant role in photocatalysis and pollutant gas detection. Despite their promising application potential, halide perovskite-based nanomaterials face challenges such as low stability, insufficient active sites, and low carrier migration effectiveness. In this review, we comprehensively discussed the research on halide perovskites for the photocatalytic removal of nitrogen oxides and volatile organic compounds (VOCs), and halide perovskites as gas sensors for gaseous pollutant detection as well as the related mechanism. Finally, we clarified the challenges and future prospects of these materials, providing new insights for advancing the development of halide perovskites in gaseous pollutant detection and photocatalytic removal.

1 Introduction

With the development of global industrialization, the contradiction between the development of human society and environmental protection has become increasingly prominent, causing people to pay more attention to serious environmental problems such as air pollution.[1–3] Pollutant

[a] *Guangdong Key Laboratory of Environmental Pollution and Health, College of Environment and Climate, Jinan University, Guangzhou, 511443, P.R. China. E-mail: yangjl@jnu.edu.cn, zhumingshan@jnu.edu.cn*
[b] *Environmental Technology, Wageningen University & Research, Wageningen, 6708 WG, The Netherlands*

gases emitted by automobiles and industry will intensify the greenhouse effect and trigger extreme weather phenomena. They will also produce fine particles in the atmosphere and lead to the formation of acid rain, adversely affecting air quality and human health. Volatile organic compounds (VOCs) serve as crucial precursors of ozone formation in the atmosphere and also contribute to haze and air pollution.[4,5] Therefore, the quest for efficient and environmentally friendly techniques to eliminate and detect gaseous pollutants has emerged as a global challenge embraced by researchers worldwide.[6,7]

The traditional air purification technique usually consumes a lot of energy and may produce by-products or

Zhijian Xiao received his Bachelor's degree from Guangzhou University in 2022. Then, he joined Prof. Mingshan Zhu's group as a Master's candidate. His current research focuses on the application of halide perovskites and porous nanomaterials in the photocatalytic purification of nitric oxide.

Zhijian Xiao

Jingling Yang received her PhD from Sun Yat-sen University. Then she worked as a postdoctoral researcher at National Taiwan University (2016–2019). Currently, she is an Associate Professor at Jinan University. Her current research focuses on the field of catalytic purification of gaseous pollutants.

Jingling Yang

4432 | *Catal. Sci. Technol.*, 2024, **14**, 4432–4449

This journal is © The Royal Society of Chemistry 2024

secondary pollutants, ultimately leading to energy waste, increased costs, and secondary pollution. Photocatalytic technology, as a green technology that could reduce energy consumption and environmental pollution, can efficiently convert gaseous pollutants into harmless substances.[8] However, the performance is still constrained by factors such as the high fabrication cost of most photocatalytic materials and the narrow photoresponse range, which restricts their application in photocatalysis.[9,10] Halide perovskites (HPs) have achieved great success in photovoltaics and optoelectronics, mainly due to their excellent photophysical properties, such as enhanced visible light absorption, long carrier diffusion length,[11,12] high carrier mobility,[13,14] high photoluminescence quantum yield,[15,16] low binding energy,[17] and tunable bandgap.[18] Halide perovskites also have attractive features such as facile synthesis method and low fabrication cost,[19,20] and are a kind of promising photocatalysts. Many researchers have begun to continually study the application of HPs and found that HPs also have excellent performance in the photocatalytic removal of gaseous pollutants. Halide perovskites not only have excellent optical properties and can be applied in the field of photocatalysis but also show high sensitivity to specific gases and superior electrical properties, which have attracted widespread attention from scientists. The halide perovskite sensor exhibits high sensitivity, selectivity, fast response/recovery time, and acceptable stability at low concentrations at room temperature.[21–24] Due to its unique advantages and ideal performance in gas detection, researchers have paid great attention to the application of halide perovskites in gas sensor research. In organometallic halide perovskites, when the perovskite is exposed to target gas molecules, its resistance decreases within seconds and recovers immediately after it leaves the atmosphere.

According to the classification of gaseous pollutants, this article summarizes the application mechanism of halide perovskites in photocatalytic removal and detection of gaseous pollutants, and introduces their latest progress in these aspects. Finally, perspectives on the future developments in those fields are given (Fig. 1).

Fig. 1 Schematic summary of photocatalytic removal and detection of gaseous pollutants.

2 Basic properties of halide perovskites

Perovskites refer to a class of compounds that have the same crystal structure as $CaTiO_3$ (ABX_3). Halide perovskites are ionic crystals with the general formula ABX_3, where A is a monovalent cation (*e.g.*, CS^+, formamidinium (FA^+)), B is a divalent metal cation (*e.g.*, Pb^{2+}, Cu^{2+}, Sn^{2+}), and X is a halogenated anion (*e.g.*, Cl^-, Br^-, I^-). The halide perovskite is an octahedral structure with the A-site cation at the apex and the B-site cation at the center of the octahedron, which cooperates with six X anions to form $[BX_6]^{4-}$ (Fig. 2a). The structure of the perovskite is constrained by the tolerance factor, which is expressed by $t = (R_A + R_B)/\sqrt{2}\,(R_X + R_B)$, where R_A, R_B, and R_X are the ionic radii of the corresponding ions. Tolerance factors (t) should be between 0.8 and 1.1. Organic cations such as methylammonium or formamidinium can occupy the A site in the perovskite structure, which is known as an organic–inorganic hybrid halide perovskite. Due to their larger size, organic cations typically cause instability in the perovskite structure, disrupting the crystal lattice and promoting ion

Mingshan Zhu received his PhD from Institute of Chemistry, Chinese Academy of Sciences (ICCAS), China. Then, he worked as a postdoctoral fellow at University of Toronto (2014–2015) and Osaka University (JSPS, 2015–2017). Currently, he is a Full Professor at Jinan University. His current research mainly focuses on the field of water pollution control chemistry.
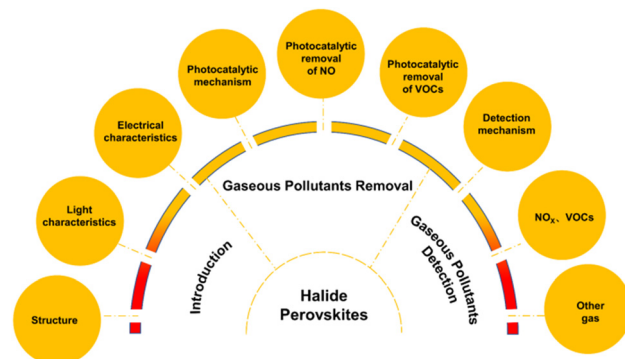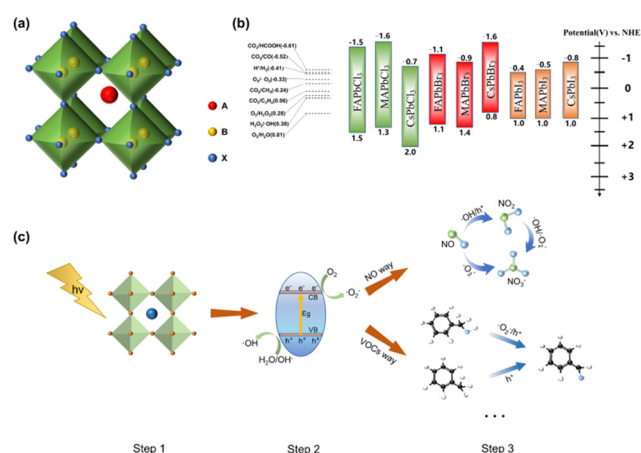
Mingshan Zhu

Fig. 2 (a) Basic structure of the perovskite. (b) Energy level structure of common halide perovskites.[18] Copyright 2015, American Chemical Society. (c) Mechanism diagram of photocatalytic removal of NO and VOCs.

migration. Replacing them with inorganic cations, such as Cs^+, significantly increases the stability, creating a pure inorganic halide perovskite. The B site is usually a Pb element, but the structure of three-dimensional lead-based perovskite is unstable, and Pb is highly toxic, tending to cause environmental pollution. Therefore, researchers have started to explore HPs with other compositional structures and compositions. Examples include A_4BX_6 (0D perovskite), AB_2X_5 (2D perovskite) and biphasic perovskite ($A_2B^+B_3^+X_6$). In the structure of biphasic perovskite, two toxic lead ions are replaced by a monovalent cation and a trivalent cation or a tetravalent cation and an empty site.[24]

For the application of halide perovskites in photocatalytic technology and gas detection devices, the relatively special optoelectronic and structural properties of these materials are important issues to be considered. The three sites A, B and X of halide perovskite all have high solid solubility. Compared with traditional single-cation perovskites, mixed-cation halide perovskites and organic halide perovskites obtained by changing the A-site element have better performance and light-harvesting ability in terms of thermal, stress, structure, and photostability.[25] For the B site, the unique atomic electronic structure of Pb is critical to the performance of the perovskite. Taking $CsPbI_3$ as an example, the Pb 6p states form the bottom of the conduction band, which exhibits triple degeneracy due to the O_h symmetry, while the top of the valence band consists of the antibonding states of the Pb 6s and I 5p states. The energy levels of occupied ns^2 states and unoccupied np^0 states can increase in the order Bi < Sb < Pb < Sn < Tl < In.[26] Such results will lead to smaller bandgaps and higher carrier mobility. Moreover, lead as an environmental toxic element can be substituted by elements with similar electronic structures and comparable ionic radii, where the bandgap can be changed close to the optimal range of the Shockley–Queisser limit.[25,27] Meanwhile, changing of halide ions at the X position or adjusting their chemical ratio can tune the bandgap of the halide perovskites. Therefore, the light absorption of halide perovskites can be tuned over a wide spectral range (from ultraviolet to near-infrared), making them more suitable for photocatalytic technologies and fluorescent gas detection devices.[28]

3 Halide perovskites for photocatalytic removal of gaseous pollutants

3.1 Photocatalytic reaction mechanism of halide perovskites

The photocatalytic mechanism of halide perovskites is similar to that of conventional semiconductors. However, halide perovskites differ from traditional semiconductors due to their unique crystal structure and surface properties, which typically exhibit high specific surface areas and abundant surface defects that can promote surface reactions and enhance photocatalytic activity. Halide perovskites act as a trap for sunlight, absorbing photons with energy equivalent to or greater than the bandgap.

This process transfers electrons from the valence band to the conduction band, leaving holes (h^+) behind and forming photogenerated electron–hole pairs. Under the influence of internal electric field forces, photogenerated electrons and holes migrate to the surface of the semiconductor and react with adsorbed oxygen and oxides to form hydroxyl radicals ($\cdot OH$) and superoxide radicals ($\cdot O_2^-$). These radicals have a strong oxidizing ability and can react with pollutants, providing a means to achieve removal and degradation. For the photogenerated carriers to better drive the photocatalytic reaction, the conduction band (CB) side of the HPs should be more negative than the reduction potential of the reacting substrate and the valence band (VB) side should be more positive than the oxidation potential of the reacting substrate. Also, considering the appropriate use of light, the bandgap should be optimal within a certain range, so the reasonable bandgap for photocatalytic applications of semiconductors should be 1.8–2.8 eV.[29] Materials with this bandgap range can absorb photon energy in the visible range and convert it into electron and hole pairs, thereby participating in photocatalytic reactions. This enables them to effectively perform photocatalytic reactions under sunlight or artificial light sources, unlike some traditional catalysts that can work only under ultraviolet light. Fig. 2b shows the energy level structures of several common halide perovskites, which are beneficial for the photocatalytic removal of NO and degradation of organic pollutants. Fig. 2c shows the mechanism of photocatalytic removal of NO and VOCs over halide perovskite catalysts. In the first step, the halide perovskite is excited by light. In the second step, photogenerated electron–hole pairs are generated, which react with adsorbed oxygen or oxides to produce $\cdot OH$ and $\cdot O_2^-$. In the third step, NO can be oxidized to NO_2 by photogenerated holes or hydroxyl radicals generated by light excitation of the halide perovskite catalyst, and NO_2 can continue to be oxidized to nitrate ions by hydroxyl groups or superoxide radicals. Volatile organic compounds can also be degraded by reacting with photogenerated electrons, photogenerated holes, and reactive oxygen species. For example, benzyl alcohol can react with superoxide radicals or photogenerated holes to form benzaldehyde. Toluene can react with photogenerated holes to form benzaldehyde as well. However, photogenerated carriers are prone to recombination when migrating to the semiconductor surfaces, which is not favorable for photocatalytic reactions.[30] Due to their defect-tolerant properties, halide perovskites are not prone to structural changes or lattice defect formation, which helps to extend the lifetime of the catalyst. This feature enables it to maintain a low defect concentration, thereby maintaining the richness and activity of catalytic active sites, and with higher carrier utilization efficiency.[31] This property plays a key role in photocatalysis and helps to achieve better photocatalytic performance.

3.2 Photocatalytic removal of NO

Fossil fuel combustion provides 80% of the world's energy demand. As a non-renewable resource, the massive use of fossil fuels not only leads to energy shortage problems but also

produces toxic gases such as NO during combustion. Emissions of NO cause photochemical smog, haze, and acid rain.[32] Removal of NO by photocatalytic conversion to NO_3^- and other products is a more environmentally friendly method. Efficient photocatalysts for NO removal have been the focus of extensive research efforts aimed at mitigating air pollution and improving air quality. However, most photocatalysts have shortcomings such as limited photoresponse (UV region), low catalytic activity, poor stability, and high NO_2 selectivity. Owing to their reasonable bandgaps and high efficiency in photogenerated carrier migration, halide perovskites have attracted attention for NO elimination.

3.2.1 Bare halide perovskite. Halide perovskites exhibit remarkable photocatalytic activity, effectively harnessing light energy to drive the degradation of gaseous pollutants. Its cost-effectiveness and ease of synthesis through simple methods make it readily available for large-scale applications. Additionally, its regenerative capabilities through synthetic techniques enhance its appeal for continuous use in environmental treatment and the remediation of gaseous pollutants. Our previous work reported $CsPbBr_3$ perovskite nanocrystals for the photocatalytic removal of NO.[33] Photographs and TEM images of $CsPbBr_3$ nanocrystals (NCs) prove that the material consists of highly crystalline nanocubes (Fig. 3a). Under visible light irradiation, $CsPbBr_3$ NCs exhibited higher photocatalytic activity for NO removal (50.6%) than g-C_3N_4 (45.8%), as shown in Fig. 3b. Stability is a key factor for practical applications. After $CsPbBr_3$ NCs were stored in an air environment for one month, the NO removal performance did not change significantly, indicating that $CsPbBr_3$ NCs had strong stability (Fig. 3c). In order to reflect the excellence of the material, the authors compared the NO_x removal performance and gas hourly space velocity (GHSV) of the $CsPbBr_3$ catalyst with that of other materials (Fig. 3d). The higher activity of $CsPbBr_3$ NCs may be due to their high electron transfer efficiency and high hole transport rate (Fig. 3e). Tang *et al.*

Fig. 3 (a) Photographs and TEM images of $CsPbBr_3$ NCs dispersed on a glass slide. (b) $CsPbBr_3$ NCs, g-C_3N_4 and blank control for photocatalytic removal of NO under visible light. (c) Stability test of $CsPbBr_3$ NCs for photocatalytic removal of NO. (d) Comparison of photocatalytic performance indicators with reported literature. (e) Reaction pathway of $CsPbBr_3$ NCs photocatalytic NO oxidation.[33] Copyright 2021, American Chemical Society.

synthesized lead-free, all-inorganic $Cs_2AgBiBr_6$ double perovskite NCs *via* a facile hot injection approach.[34] $Cs_2AgBiBr_6$ showed an octahedral double perovskite structure, in which the two toxic Pb^{2+} ions of $CsPbBr_3$ are replaced by one Ag^+ and one Bi^{3+} ion. After visible light irradiation for 30 minutes, the NO removal rate of the prepared $Cs_2AgBiBr_6$ NCs was as high as 90%. After washing, $Cs_2AgBiBr_6$ NCs can wash away the products on the surface and restore the original active sites, so the NO removal rate is as high as 97%. Under the same conditions, the NO conversion rate of $CsPbBr_3$ NCs is only about 34%. $Cs_2AgBiBr_6$ NCs can generate electron–hole pairs when excited by visible light photons with energy equal to or greater than the bandgap. Photogenerated electrons can reduce the O_2 adsorbed on the catalyst to superoxide radicals, and then NO reacts with the superoxide radicals to generate the final products HNO_2 and HNO_3. In addition, photogenerated electrons can also reduce O_2 to H_2O_2, which can be further converted into hydroxyl radicals after capturing the electrons. Afterward, NO reacts with hydroxyl radicals to generate NO_2, and the photogenerated holes in the valence band can also directly oxidize NO.

3.2.2 Halide perovskites and silica-containing composites. The synthesis method of bare halide perovskite catalysts is relatively simple, and the photocatalytic process proceeds under relatively mild conditions. This makes halide perovskites more widely used. However, the light absorption range of bare halide perovskite is limited, the photogenerated carriers are easily recombined, and the stability is poor. Therefore, the photocatalytic performance can be enhanced by compounding with other materials. Silicon dioxide provides a stable substrate, and anchoring photocatalytic materials to silica improves their stability and durability. It can protect the active ingredients from degradation or aggregation. This improved stability extends the life of the photocatalyst. Silica materials can also control the morphology and dispersion of anchored photocatalytic components. By adjusting parameters such as particle size, shape and loading density, the effective surface area for photocatalytic reactions can be increased, thereby improving activity.[35] Anchoring halide perovskites on silica materials is undoubtedly an effective means of improving photocatalytic performance. In our previous work, we reported a nanomembrane (CBB@SBA($\perp$)) confining $Cs_3Bi_2Br_9$ nanocrystals in vertical channels of porous insulating silica flakes for photocatalytic reduction of nitric oxide emission.[36] Our synthesized CBB@SBA($\perp$)porous membrane has high porosity, low tortuosity ($\tau \approx 1$) and ultra-short channel length of vertical nanochannels, which can achieve effective mass transfer. The silica film, acting as an insulator, maintains high light transmittance and a relatively concentrated internal electric field in a confined space, thereby enhancing the catalytic effect of the photocatalyst. Under simulated solar light, CBB@SBA($\perp$) exhibited a record-breaking photocatalytic NO conversion efficiency of 98.2% and an extremely low selectivity for toxic NO_2 of only 5.2%. Huang *et al.* synthesized $FAPbBr_3$/A-SiO_2 nanocomposite photocatalysts by N–H chemical bonding, anchoring formaldehyde lead halide perovskite quantum dots on aminated silica spheres.[37] The
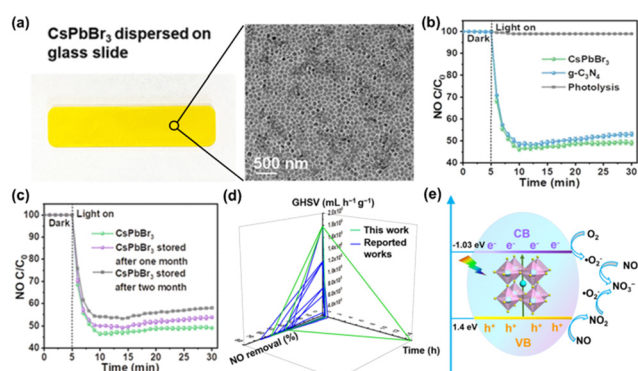
This journal is © The Royal Society of Chemistry 2024

Catal. Sci. Technol., 2024, **14**, 4432–4449 | **4435**

introduction of A-SiO$_2$ provided a larger BET surface area for the composite. On the surface of A-SiO$_2$, abundant NH$_x$ groups provide nucleation and growth sites for halide perovskite quantum dots, making the FAPbBr$_3$ quantum dots more dispersed to avoid agglomeration and thus obtaining more photocatalytic active sites. FAPbBr$_3$ quantum dots are evenly distributed on the surface of silicon spheres (Fig. 4a). The activity of the material for NO removal in the first half hour under visible light (70%) was significantly higher than that of pristine FAPbBr$_3$ (30%) (Fig. 4b). The significant improvement in NO removal efficiency reflects the key role of the N–H chemical bond, enabling efficient and rapid separation of carriers and efficient photocatalytic removal of NO. The author conducted three cycle experiments to evaluate the stability and recyclability of the catalyst (Fig. 4c). The NO removal rates of the three photocatalytic performance experiments were 70%, 60%, and 57%, respectively. The photocatalytic mechanism of FAPbBr$_3$/A-SiO$_2$ composite material under light irradiation is proposed in Fig. 4d. Under illumination, the photogenerated electrons on the VB of FAPbBr$_3$ are excited to the CB, leaving photogenerated holes on the VB.[38] Photogenerated holes will be transferred to the catalyst surface and react with OH$^-$ ions or water to generate ·OH, while photogenerated electrons can react with O$_2$ to generate ·O$_2^-$. These reactive oxygen species can serve as oxidants in the reaction.

3.2.3 Heterojunction engineering. Although halide perovskites have suitable bandgaps, recombination of their photogenerated carriers is still a bottleneck that influences the photocatalytic performance. A heterojunction catalyst is a hybrid material which is an interface composed of two or more semiconductors with different bandgaps. Since the band potentials of different semiconductor structures are not equal, electrons and holes in semiconductors can be effectively separated by constructing a heterojunction catalyst, and the

recombination rate of photogenerated carriers is reduced. Secondly, semiconductors with lower redox potential are prone to redox reactions, leading to selective redox reactions in heterojunction photocatalysts.[39] Therefore, heterojunction engineering is an effective means to improve the photocatalytic removal of NO by halide perovskites.

Dong *et al.* reported a series of Cs$_3$Bi$_2$Cl$_9$/(BiO)$_2$CO$_3$ heterojunctions (abbreviated as C–B-*X*, *X* = 0.5, 1, 3).[40] Here, C and B represent Cs$_3$Bi$_2$Cl$_9$ and (BiO)$_2$CO$_3$, respectively. By weight percentage, the material was prepared through the electrostatic self-assembly of CBC (Cs$_3$Bi$_2$Cl$_9$) and BOC ((BiO)$_2$CO$_3$). Fig. 5a shows a schematic of the material synthesis and an overview of the photocatalysis. The introduction of CBC QDs to the BOC surface resulted in significantly improved photocatalytic performance. C–B-1 achieved a 55% NO purification rate in about 5 minutes, while BOC achieved only a 34% NO purification rate within 5 minutes of visible light irradiation (Fig. 5b). The binding energy of Bi 4f, C 1s and O 1s in C–B-1 shifts to a higher energy level than that of the original BOC, while the negative charge of Bi 4f and Cl 2p of C–B-1 increases compared to that of pure CBC QDs, indicating hybridization in the unexcited state. When electrons are transferred from BOC to CBC, this direct charge transfer at the interface generates an internal electric field at the two-phase interface, effectively separating
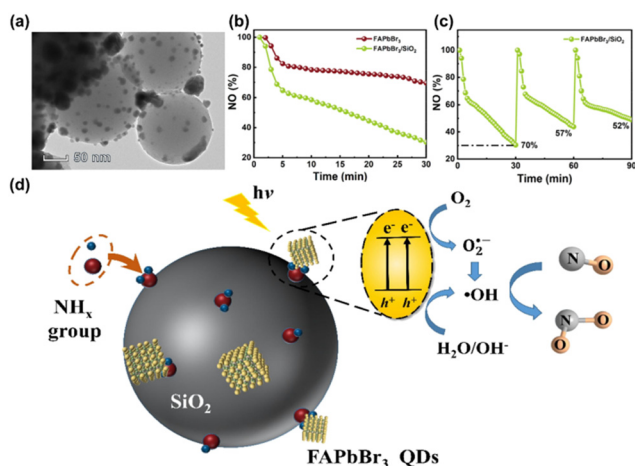

Fig. 4 (a) TEM image of FAPbBr$_3$/A-SiO$_2$ composites. (b) FAPbBr$_3$ and FAPbBr$_3$/A-SiO$_2$ for photocatalytic removal of NO under visible light conditions. (c) The stability of FAPbBr$_3$/A-SiO$_2$ was tested under visible light conditions. (d) Schematic diagram of the photocatalytic mechanism of NO photocatalytic removal by FAPbBr$_3$/A-SiO$_2$.[37] Copyright 2020, Elsevier.
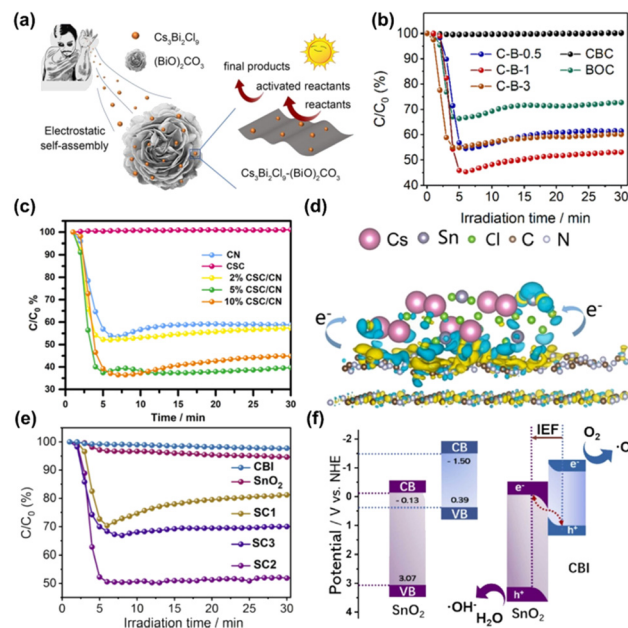

Fig. 5 (a) A schematic diagram of the synthesis of Cs$_3$Bi$_2$Cl$_9$ QD supported on (BiO)$_2$CO$_3$ and an overview of photocatalysis. (b) Visible light photocatalytic removal of NO was performed on (BiO)$_2$CO$_3$, Cs$_3$Bi$_2$Cl$_9$ QD and C–B-*X* (*X* = 0.5, 1, 3) samples.[40] Copyright 2021, Elsevier. (c) Comparison of the photocatalytic NO removal performance of the prepared samples. (d) Charge difference distribution between Cs$_2$SnCl$_6$ and C$_3$N$_4$.[41] Copyright 2022, Elsevier. (e) Visible light photocatalytic performance on SnO$_2$, Cs$_3$Bi$_2$I$_9$ and SC*X* nanoheterostructures. (f) Diagram of the photoelectron charge transfer process at the interface of SnO$_2$/Cs$_3$Bi$_2$I$_9$ heterostructures.[42] Copyright 2022, Elsevier.

4436 | *Catal. Sci. Technol.*, 2024, **14**, 4432–4449

This journal is © The Royal Society of Chemistry 2024

carriers and promoting more photocatalytic charges to participate in the photocatalytic process. Dong *et al.* successfully synthesized a Cs_2SnCl_6/C_3N_4 (abbreviated as CSC/CN) heterojunction photocatalyst using the solid-phase grinding method.[41] After constructing the CSC/CN heterostructure, the photocatalytic behavior of the CSC/CN heterojunctions was improved with various compound ratios (2%, 5%, and 10%). Among them, the most significant performance improvement is exhibited by the 5% CSC/CN heterojunction. When CSC/CN was irradiated with visible light for 30 minutes, its photocatalytic purification rate of NO removal reached 60.3%, which was significantly higher than that of the original C_3N_4 (Fig. 5c). To better understand the mechanism of the reaction, the authors used density functional theory (DFT) calculation methods to study the interaction between the CSC and CN interface. Fig. 5d demonstrates the transfer of electrons on CN to CSC through the interfacial channel. The transfer of electrons induces an internal electric field between the interfaces, promoting their interaction. This interaction facilitates carrier separation, leading to the generation of more free electrons and accelerating the photocatalytic reaction process.

To better suppress the recombination of photogenerated carriers, two coupled semiconductors (PC I and PC II) with staggered band alignment can be combined to form a type II heterojunction, so that the photogenerated electrons and holes can be collected in different semiconductors. In a type II heterojunction, the CB and VB positions of PC I are higher than those of PC II. Under light, both PC I and PC II are photoexcited to generate electron–hole pairs. The photogenerated electrons from PC I with high CB will migrate and accumulate on PC II with low CB, while the holes from PC II will transfer to PC I. The photogenerated electrons on PC II can undergo reduction reactions, and the photogenerated holes on PC I can undergo oxidation reactions. Since the electrons and holes are collected in different semiconductors, charge recombination can be effectively suppressed. Therefore, constructing a type II heterojunction with HPs and other semiconductors is an effective way to improve the photocatalytic removal of NO. Lu *et al.* synthesized $FAPbBr_3/g-C_3N_4$ heterojunctions (abbreviated as FA/CN) *via* one-pot synthesis at room temperature for photocatalytic NO removal.[43] In comparison to pure $FAPbBr_3$ and pure $g-C_3N_4$, the NO removal efficiency of this composite is significantly better. The highest removal rate of FA/CN for 600 ppb NO was 58%. A conventional type II heterojunction is formed between $FAPbBr_3$ and $g-C_3N_4$ because their energy band structures are matched. This can be explained by the composition of a type II heterojunction. Photogenerated electrons in the conduction band of $FAPbBr_3$ migrate easily to the conduction band of $g-C_3N_4$, while photogenerated holes in the valence band of $g-C_3N_4$ migrate spontaneously to the valence band of $FAPbBr_3$. This type II heterojunction behavior greatly improves the separation and transfer efficiency of photogenerated electron–hole pairs by inducing electrons and holes to move in opposite directions. It also reduces the possibility of electron–hole pair recombination.

Numerous studies confirm that in-plane charge localization and directed linear charge migration can play an important role in photocatalytic applications.[44,45] From a thermodynamic point of view, the improvement of charge separation efficiency in type II heterojunctions comes at the expense of reduced redox ability, which is unfavorable in photocatalytic reactions. In a typical type II heterojunction, photogenerated electrons and holes accumulate on the CB of oxidation photocatalysts and the VB of reduction photocatalysts, respectively, resulting in weak redox ability. In an S-type heterojunction, the CB of reduction photocatalysts and the VB of oxidation photocatalysts accumulate a large number of photogenerated electrons and holes, respectively, and have strong redox ability, while other photogenerated carriers will be recombined. Therefore, Zhong *et al.* synthesized an S-type heterojunction of $Cs_3Bi_2I_9/SnO_2$ double quantum dots, providing a solution to the problems of lack of reactive centers, easy recombination of photogenerated carriers, and low light utilization.[42] SnO_2, $Cs_3Bi_2I_9$ and $Cs_3Bi_2I_9/SnO_2$ (abbreviated as SC*X*, *X* = 1, 2, 3) samples have obvious differences in NO removal rate within 30 minutes. The NO removal rate of SnO_2 is only 6%, and the NO removal rate on $Cs_3Bi_2I_9$ HPQDs (halide perovskite quantum dots) is also negligible. When the ratio of $Cs_3Bi_2I_9$ to SnO_2 reaches 20% (SC2), the NO removal rate reaches a maximum of around 50%, approximately 17 times and 8 times higher than the removal rates of $Cs_3Bi_2I_9$ and SnO_2 alone, respectively (Fig. 5e). The modulation of the interface internal electric field (IEF) and bending band in the synthesized S-scheme heterostructure facilitates the separation and directional transfer of photogenerated carriers between the two semiconductors. This ultimately results in the enrichment of the photoexcited electrons and holes in the conductor of $Cs_3Bi_2I_9$. The bands of SnO_2 facilitate the catalyst's capacity to sustain high redox levels, producing abundant $\cdot O_2^-$ and $\cdot OH$ radicals for subsequent photocatalytic reactions, as depicted in Fig. 5f. When it comes to SnO_2, NO molecules initially cling to the catalyst surface through bidentate and monodentate modes, while the H_2O molecules that are absorbed are later stimulated and separated into hydroxides. The transitional species can then be further oxidized to create nitrates or other components. Due to the low productivity of hydroxyl radicals, intermediates can accumulate in large quantities. However, the $Cs_3Bi_2I_9/SnO_2$ double quantum dot nanoheterostructure is distinct in this regard. The NO molecules primarily adsorb to the surface of the double quantum dots through the bidentate mode. Thus, the system enables efficient management of competing reactions. The findings suggest that the tightly confined active interface between the $Cs_3Bi_2I_9$ and SnO_2 quantum dot phases in this dual quantum dot model can increase the transmission efficiency while limiting the transmission distance. Additionally, it can facilitate the direct and effective involvement of photogenerated electrons and holes in photocatalysis, resulting in the conversion of activated reactants into active groups, thus enhancing the photocatalytic performance.

This journal is © The Royal Society of Chemistry 2024

Catal. Sci. Technol., 2024, **14**, 4432–4449 | **4437**

3.3 Photocatalytic removal of VOCs

Volatile organic compounds include aliphatic, aromatic, oxygen-containing, halogen-containing, nitrogen-containing hydrocarbons, and sulfonyl compounds. Their sources can be categorized into natural and anthropogenic sources. Natural releases consist of uncontrollable emission sources such as forest fires and green vegetation, while anthropogenic sources include fuel combustion, transportation, coal, natural gas, and other combustion sources. Most VOCs possess an unpleasant odor and are toxic, irritating, teratogenic, and carcinogenic, especially benzene, toluene, and formaldehyde, which can pose significant health risks to humans. The utilization of photocatalytic technology to degrade volatile organic pollutants is environmentally friendly. Photocatalytic processes typically involve converting volatile organic compounds into less harmful substances such as water vapor, carbon dioxide, and mineralization by-products. Halide perovskites can be designed to selectively target specific VOCs, minimizing the production of by-products and improving the overall efficiency of pollutant degradation, thereby not only reducing the generation of secondary pollutants but also contributing to more efficient air purification.

3.3.1 Bare halide perovskite. Halide perovskite materials, renowned for their exceptional light-absorbing capabilities and fast carrier dynamics, have attracted increasing attention as potential photocatalysts for the degradation of volatile organic pollutants. Although bare halide perovskite catalysts have shown good prospects in photocatalytic degradation of VOCs, they still have problems such as low stability and insufficient performance in photocatalytic applications. Therefore, researchers continue to explore the application of photocatalytic removal of VOCs in a wider range of scenarios and simpler conditions. Current research is diligently focused on solving these challenges to improve the performance of bare halide perovskite catalysts.

Gimenez et al. utilized the potential of $CsPbBr_3$ quantum dots for the photocatalytic and photoelectrochemical oxidation of 2-mercaptobenzothiazole (MBT).[46] They also investigated the materials' suitability for the degradation of organic compounds through photocatalytic and photoelectrochemical means. $CsPbBr_3$, $CsPbI_3$, $CsPb_{0.4}Sn_{0.6}I_3$, and $CsPb(Br_{0.5}I_{0.5})_3$ were synthesized using the hot injection method. Elevation of the iodine/bromine ratio or cation exchange at the B-site of the ABX_3-type structure, leading to a decrease in the bandgap. These nanocrystals exhibit high luminescence under ultraviolet light irradiation (Fig. 6a), and a similar trend was observed in the photoluminescence of each tested material (Fig. 6b). The authors conducted control tests with and without quantum dots and UV filters as well as without both, aiming to elucidate the role of halide perovskite quantum dots in the photodegradation process of MBT. The results indicate that in the absence of $CsPbBr_3$ quantum dots, only UV light is effective in the degradation of MBT, with no reaction occurring in the absence of light or in
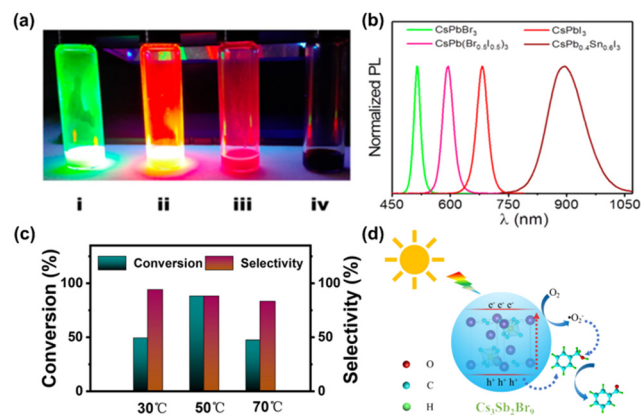

Fig. 6 (a) Photographs under UV light: (i) $CsPbBr_3$, (ii) $CsPbI_3$, (iii) $CsPb(I_{0.5}Br_{0.5})_3$, and (iv) $CsPb_{0.4}Sn_{0.6}I_3$. (b) PL spectra of different perovskite quantum dots.[46] Copyright 2019, American Chemical Society. (c) Performance diagram of the photocatalytic oxidation of benzyl alcohol by $Cs_3Sb_2Br_9$ samples at different synthesis temperatures under O_2 atmosphere. (d) Schematic diagram of the reaction pathway of $Cs_3Sb_2Br_9$ photocatalytic oxidation of benzyl alcohol to benzaldehyde.[47] Copyright 2022, Elsevier.

the presence of visible light. Both UV and visible light degradation rates are significantly accelerated in the presence of $CsPbBr_3$ quantum dots. This study demonstrates that the excellent photovoltaic performance of halide perovskite quantum dots, when utilized as dispersed nanoparticles, can be harnessed for photocatalysis and the photochemical degradation of organic compounds. Tang et al. used a simple antisolvent method to synthesize highly crystalline all-inorganic halide perovskite $Cs_3Sb_2Br_9$ microcrystals at varying temperatures.[47] Under visible light irradiation and an oxygen atmosphere, the material demonstrates a conversion rate of up to 77% and a benzaldehyde selectivity of up to 88% for the photocatalytic oxidation of benzyl alcohol. Even more attractive is the conversion of 96% and the selectivity of 94% under optimized conditions in air atmosphere (Fig. 6c). When light shines on $Cs_3Sb_2Br_9$, electrons and holes are generated and transferred. The photogenerated electrons of $Cs_3Sb_2Br_9$, when excited from the valence band to the corresponding conduction band, form photogenerated carriers. These carriers combine with the adsorbed O_2 molecules in the air, resulting in the production of superoxide radicals, a key substance. Furthermore, the holes in the valence band can activate the adsorbed benzyl alcohol. Superoxide radicals react with activated benzyl alcohol to produce the final product benzaldehyde (Fig. 6d).

Oron et al. used the Goldschmidt tolerance factor to predict the stability of the synthesized double perovskite $Cs_2Au^IAu^{III}X_6$ and conducted a photocatalytic toluene degradation reaction.[48] The results show that the toluene removal efficiencies of $Cs_2Au_2Cl_6\_5$ and $Cs_2Au_2Cl_6\_2$ (samples of different elemental compositions) under UV light irradiation are approximately 29% and 32%, while the photodegradation efficiencies of $Cs_2Au_2Cl_6\_5$ and $Cs_2Au_2Cl_6\_2$ for toluene under visible light are approximately 35%

4438 | Catal. Sci. Technol., 2024, **14**, 4432–4449

This journal is © The Royal Society of Chemistry 2024

and 58%, respectively. To study the electronic structural properties of various configurations of mixed halide Cs_2Au^I-$Au^{III}X_6$ perovskites, the authors conducted DFT calculations. The influence of the choice of halide (X = Cl, Br, I) and crystal phase was investigated. The better photocatalytic performance of $Cs_2Au_2Cl_6\_2$ may be due to its higher purity (less gold nanoparticles), which does not cause aggregation of gold nanoparticles and thus becomes a channel for photogenerated carrier recombination. Chen *et al.* replaced Bi with Sb to obtain a layered structure of $Cs_3Bi_{1.8}Sb_{0.2}Br_9$.[49] It improves the photocatalytic performance of selective oxidation of toluene by increasing the light absorption capacity and achieving effective carrier separation. $Cs_3Bi_{1.8}$-$Sb_{0.2}Br_9$ is synthesized after doping with a small amount of Sb, which can accelerate the $C(sp^3)$–H bond dissociation and promote the generation of photogenerated holes. Density functional theory calculations were used to further investigate the effect of Sb doping on h^+ generation. The difference in charge between the top layer and the bottom layer of $Cs_{12}Bi_7Sb_1Br_{36}$ is significant. The electrons in the Sb-containing layer are 0.2 e lower than the electrons in the other layer, indicating that photogenerated holes accumulate on the Sb side. The charge difference of the other samples is less than 0.05 e. Under visible light irradiation, the conversion rate of toluene reaches 5.83 mmol g^{-1} h^{-1}. The possible photocatalytic principle is that toluene is first adsorbed on the surface of $Cs_3Bi_{1.8}Sb_{0.2}Br_9$ through the $-CH_3$ group and the H atom of benzene. Under visible light irradiation, photogenerated holes oxidize toluene to form a benzyl group, and at the same time photogenerated electrons reduce the adsorbed O_2 to $\cdot O_2^-$. The benzene free radical is then oxidized by the superoxide radical to form a peroxyl radical, which combines with a proton to form $PhCH_2O_2$-H and then dehydrated to form benzaldehyde.

3.3.2 Halide perovskite-based composite. The synergistic effect among different components in the complex can increase the efficiency of capturing and utilizing light energy to degrade pollutants. Composite materials with other materials can expand the absorption range to cover a wider spectrum and can also enhance the stability of halide perovskites. Dai *et al.* reported that $Cs_3Bi_2Br_9$ nanoparticles loaded onto SBA-15 exhibited excellent aliphatic and aromatic $C(sp^3)$–H bond activation properties under visible light irradiation.[50] When the loading rate of $Cs_3Bi_2Br_9$ is 10 wt%, the $Cs_3Bi_2Br_9$/SBA-15 photocatalyst exhibits the highest conversion rate of 12 600 μmol g_{cat}^{-1} h^{-1}, and the selectivity for benzaldehyde is as high as 90% (with alcohol as the main by-product). The 5 wt% $Cs_3Bi_2Br_9$/SBA-15 photocatalyst exhibited lower reactivity, which may be due to the lower number of active centers and weak light absorption capability of the catalyst. In contrast, at higher loading levels (20 and 40 wt%), the activity of the catalyst towards toluene decreased sharply, mainly because of the limited number of active sites and severe charge reorganization caused by nanoparticle aggregation. Li *et al.* reported a one-pot synthesis of surface-modified $CsPbBr_3/Cs_4PbBr_6$ nanosheets based on ligand-

assisted precipitation (LARP) and modified the $CsPbBr_3/Cs_4$-$PbBr_6$ nanosheets with $ZrCl_4$ to improve the oxidation capability of the photocatalyst and promote vector transfer.[51] The photocatalytic performance of the catalyst was investigated by photocatalytic oxidation of styrene, and the results showed that the yield of CPB was 372 μmol g^{-1} h^{-1}. As the amount of $ZrCl_4$ increases, the maximum yield of CPB-Zr-0.75 is 1098 μmol g^{-1} h^{-1} (Fig. 7a). The reaction process may be that visible light activates excitons in CPB, and styrene is adsorbed on the surface of CPB and oxidized by photogenerated holes into the corresponding cationic radicals. These radicals are then oxidized to benzaldehyde by reactive oxygen species (Fig. 7b). Huang *et al.* synthesized $FAPbBr_3/TiO_2$ composite materials through a room temperature antisolvent precipitation method.[52] The photocatalytic ability of the material was evaluated by selective photocatalysis of benzyl alcohol in a polar solvent (toluene). As seen in Fig. 7c, both pure $FAPbBr_3$ and TiO_2 (10 mg) showed approximately 15% conversion (0.1 mmol benzyl alcohol in 2.5 mL toluene) after 8 hours of illumination. The photocatalytic activity of pure TiO_2 was doubled by the addition of 1 wt% $FAPbBr_3$. The 15 wt% $FAPbBr_3/TiO_2$ composite material has the highest photocatalytic conversion rate of benzyl alcohol, reaching 63%, which is 4 times higher than that of a single catalyst material. $FAPbBr_3$ content exceeding 15 wt% will reduce the conversion rate. The possible reason is that increasing the amount of perovskite precursor leads to the increase of $FAPbBr_3$ nanocrystals, which leads to the coverage of the TiO_2 surface and reduces the surface area of TiO_2 exposed to the reagent solution. Eventually, the carrier movement distance becomes longer, which reduces the charge separation efficiency. The photogenerated electrons of the perovskite will gather into TiO_2 and activate O_2 to form $\cdot O_2^-$, thereby achieving excellent
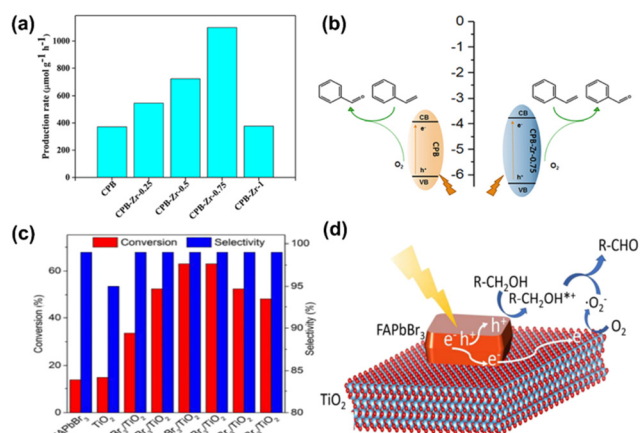

Fig. 7 (a) Photocatalytic performance diagrams of CPB and CPB-Zr-*x* (*x* = 0.25, 0.5, 0.75, 1). (b) The reaction scheme of photocatalytic oxidation of styrene to benzaldehyde.[51] Copyright 2020, Frontiers. (c) Photocatalytic oxidation of benzyl alcohol by pure $FAPbBr_3$, TiO_2, and a series of $FAPbBr_3/TiO_2$ mixtures. (d) Selective photocatalytic oxidation of benzyl alcohol to benzaldehyde using a $FAPbBr_3/TiO_2$ hybrid system.[52] Copyright 2018, American Chemical Society.

This journal is © The Royal Society of Chemistry 2024

Catal. Sci. Technol., 2024, **14**, 4432–4449 | **4439**

photocatalytic activity and increasing the photocatalytic efficiency by 4 times, as shown in Fig. 7d.

3.3.3 Heterojunction engineering. Combining halide perovskites with other semiconductors may result in the formation of heterojunctions with more active sites. In order to form a heterojunction between halide perovskites and other materials, the conduction band and valence band energy levels need to be matched, the lattice structure should also be matched to a certain extent, and the lattice constants should be similar, which helps to reduce the strain energy caused by lattice mismatch. The optical properties of this heterojunction can be tuned to expand the spectral response range, allowing the photocatalyst to utilize a wider range of light energy to achieve catalytic activity. Furthermore, these heterojunctions show improved charge separation and utilization efficiency, ultimately improving the overall photocatalytic performance. Therefore, combining halide perovskites with other materials not only increases the available active sites but also enhances the versatility and effectiveness of the photocatalytic system, providing ample opportunities for VOCs to interact with the photocatalysts under various reaction conditions.

Yang *et al.* reported that lead-free all-inorganic perovskite $Cs_3Bi_2Br_9$ NCs were uniformly distributed on the surface of ultrathin two-dimensional (2D) single-layer $Ti_3C_2T_X$ MXene nanosheets in an *in situ* growth manner.[53] A tight heterostructure is formed between the prepared $Cs_3Bi_2Br_9$ NCs and $Ti_3C_2T_X$ MXene, which not only significantly enhances the performance of $Cs_3Bi_2Br_9$ NCs in the photocatalytic oxidation of aromatic hydrocarbons and aliphatic alkanes under visible light irradiation but also greatly improves the stability of $Cs_3Bi_2Br_9$ NCs in the reaction environment. When the reaction time is extended from 4 h to 20 h, the photooxidation activity of the catalyst is stronger, and the conversion rate of toluene into benzaldehyde has no obvious loss. Under the same conditions, when pristine $Cs_3Bi_2Br_9$ NCs were used as photocatalysts, the conversion rate dropped sharply, with a loss of 40% after 20 h. Photogenerated electrons can reduce O_2 to $\cdot O_2^-$ on the surface of $Ti_3C_2T_X$ MXene, and the utilization rate of photogenerated holes on the $Cs_3Bi_2Br_9$ NCs VB is also greatly enhanced, which is effective in promoting the oxidation of alkane substrates to carbon-centered radicals (R–C$^\cdot$), and react with $\cdot O_2^-$ to generate the corresponding aldehyde.

By constructing a type II heterojunction, long-lived carriers and a wide spectral response can be obtained, allowing the catalyst to more effectively utilize light energy during the photocatalytic removal of VOCs, thereby generating more active oxygen species to react with VOCs and achieve the purpose of purifying VOCs. Luo *et al.* reported a type II heterojunction, $FAPbBr_3/C_3N_4$ heterojunction, photocatalyst that can efficiently and selectively catalyze the oxidation of benzyl alcohol through photocatalysis.[54] By exploiting the energy band alignment of photoelectrons/holes in the $FAPbBr_3/C_3N_4$ hybrid material and modifying the ratio between the two materials, an optimized photocatalytic

performance under visible light was achieved. The heterojunction photocatalyst formed by g-C_3N_4 and $FAPbBr_3$ exhibits highly stable and efficient photocatalytic ability in oxidizing benzyl alcohol to produce aldehydes. Compared with the original $FAPbBr_3$, its photocatalytic efficiency is increased by 3 times. Yin *et al.* employed a straightforward electrostatic self-assembly technique to fabricate a 2D/2D (2D: two-dimensional) $Cs_3Bi_2Br_9$/g-C_3N_4 heterojunction.[55] By constructing a type II heterostructure, the recombination of the photogenerated electrons and holes can be reduced, thereby extending the lifetime of photogenerated carriers and improving photocatalytic effects. Under visible light irradiation, the highest production rate of benzaldehyde from the oxidation of toluene is 4.53 mmol h^{-1} g^{-1} when the ratio of $Cs_3Bi_2Br_9$/g-C_3N_4 exceeds 10%. The rate of toluene oxidation to benzaldehyde is 41.8 times and 2.3 times higher than that of g-C_3N_4 and $Cs_3Bi_2Br_9$ nanosheets, respectively, and the selectivity to benzaldehyde is as high as 90% (Fig. 8a). The VB and CB positions of $Cs_3Bi_2Br_9$ and g-C_3N_4 indicate that they can form type II heterojunctions (Fig. 8b). These may be the reasons for the increased activity and stability of the material. (i) The formation of a 2D/2D type II heterojunction structure promotes the generation of key active substances and intermediates, allowing for better electron–hole separation and reducing their recombination
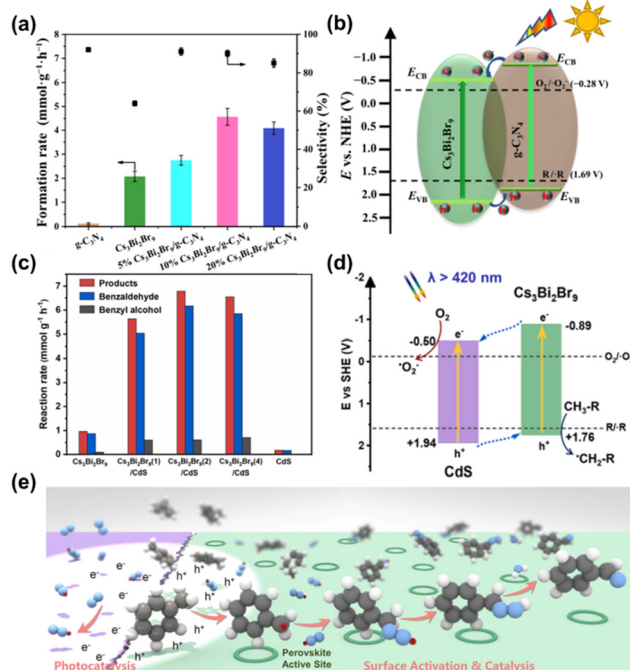

Fig. 8 (a) Photocatalytic oxidation of toluene over g-C_3N_4, $Cs_3Bi_2Br_9$, and $Cs_3Bi_2Br_9$/g-C_3N_4. (b) Band structures of the composite photocatalyst.[55] Copyright 2022, Springer Nature. (c) Photocatalytic activity of $Cs_3Bi_2Br_9$/CdS, $Cs_3Bi_2Br_9$ and CdS for photocatalytic oxidation of toluene. (d) Schematic representation of the band structure and redox reactions of $Cs_3Bi_2Br_9$ and CdS. (e) Schematic diagram of the photocatalytic pathway for the conversion of aromatic C(sp^3)–H and oxygen at the active site of perovskite materials.[58] Copyright 2022, Elsevier.

4440 | *Catal. Sci. Technol.*, 2024, **14**, 4432–4449

This journal is © The Royal Society of Chemistry 2024

rate, thereby improving activity. (ii) The introduction of g-C_3N_4 alters the reaction pathway and improves selectivity towards benzaldehyde.[56,57] (iii) There is a strong interaction between g-C_3N_4 and $Cs_3Bi_2Br_9$, and the increase in its electron cloud density will lead to a decrease in surface tension. Therefore, the presence of g-C_3N_4 reduces the surface energy of $Cs_3Bi_2Br_9$ and improves its stability.

Zou *et al.* investigated the photocatalytic efficiency of toluene removal over the synthesized $Cs_3Bi_2Br_9$/CdS composite.[58] Compared with original CdS (0.18 mmol g^{-1} h^{-1}) and $Cs_3Bi_2Br_9$ (0.97 mmol g^{-1} h^{-1}), the optimized activity was as high as 6.79 mmol g^{-1} h^{-1}, which was increased by 37.6 times and 7.1 times, respectively (Fig. 8c). The active sites on the surface of halide perovskites are a new type of heterostructure photocatalyst that provide a thermodynamically and kinetically more favorable reaction pathway for the conversion of key intermediates. In addition to the formation of heterojunction structures and appropriate energy band positions to improve charge separation, a new and highly effective surface catalytic process for converting benzene radicals and superoxide anions into aldehydes on the surface of $Cs_3Bi_2Br_9$ derivatives was observed and demonstrated. The experimental results show that charge separation is not the main function of $Cs_3Bi_2Br_9$, and the author believes that the surface activation of intermediate free radicals converted on $Cs_3Bi_2Br_9$ is reasonable (Fig. 8d). A schematic diagram of photo-surface synergistic catalysis for the conversion of aromatic C(sp^3)–H with oxygen is shown in Fig. 8e. The process includes a redox step driven by e^-/h^+ induced by high-energy light and the surface on the perovskite active site.

4 Applications of halide perovskites in gas sensing

4.1 Mechanism of gas sensing over halide perovskites

A chemical sensor is a device that senses a specified measured substance and converts it into chemical information according to certain laws. The above-mentioned chemical information may come from the chemical reaction of the substance being analyzed or from the physical properties of an analyzed system.[59] Chemical sensors typically consist of two main components: a receptor for detecting the target substance and a signal transducer. Semiconductor gas sensors are categorized according to their sensitivity mechanism and are generally divided into non-resistive and resistive types. Resistive sensors rely on changes in electric resistance to indicate gas sensitivity characteristics. Non-resistive gas sensors, such as electrochemical gas sensors, promote a chemical reaction on the surface of the gas-sensitive electrode, which results in a change in electrode charge. The change in charge generates electrical signals by which the composition and concentration of the gas can be determined. By utilizing these different sensing mechanisms, chemical sensors

provide versatile solutions for detecting and quantifying various gases in a variety of applications.

Halide perovskite gas sensors exhibit better sensitivity, selectivity, stability and reliability that can be applied to detecting a wide range of gaseous pollutants.[60] The interaction between halide perovskites and their hybrid materials with detected gas molecules not only influences the color, photostability, and physicochemical properties of the materials but also significantly impacts their optical and photovoltaic properties. Optical property-related gas sensors can consist of a perovskite layer deposited on a material A layer (*e.g.*, TiO_2) on an underlying fluorine-doped tin oxide (FTO) glass substrate (Fig. 9a). The top electrode is connected to the top surface of the perovskite layer through probe B (*e.g.*, Au), while the bottom electrode is interconnected with the top electrode, allowing gas molecules to come into contact with most of the material's surface. Under light irradiation, the perovskite layer generates electron–hole pairs. Subsequently, the photogenerated electrons transferred from the CB of the perovskite material are transferred to the FTO through the A layer, while the VB holes of the perovskite material are gathered at the B probe, leading to a net current flowing from the FTO to Au through the output circuit without applying any external bias. The generated photocurrent is used to effect changes in the electrical properties of the perovskite-based detection device caused by interactions with gas molecules.

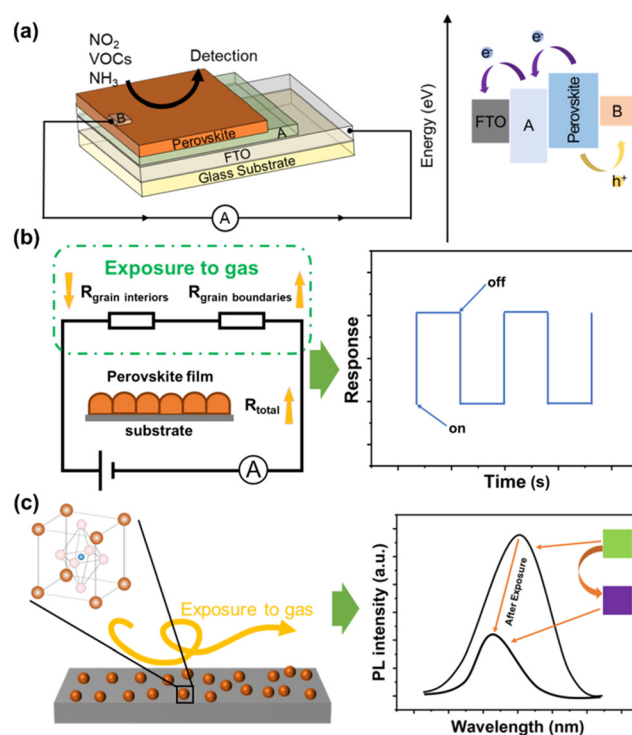**Fig. 9** (a) Schematic diagram of chemical sensor layout. (b) Schematic diagram of electrical signal changes after exposing the target gas and turning off the target gas. (c) Schematic diagram of PL intensity and material color changes after exposure to target gas.[61] Copyright 2017, Elsevier.

This journal is © The Royal Society of Chemistry 2024

Catal. Sci. Technol., 2024, **14**, 4432–4449 | **4441**

Halide perovskite capacitive gas sensors operate on the principle of changes in capacitance when the sensor device is exposed to a specific gas. The sensing mechanism involves changes in the electrical properties of the perovskite material due to interaction with the target gas. When a halide perovskite sensing layer comes into contact with a target gas, interactions occur between the gas molecules and the surface or bulk of the perovskite material. These interactions may involve adsorption, desorption, or chemical reactions. If gas adsorption causes an increase in carrier concentration or conductivity within the perovskite layer, it can affect the effective dielectric constant and thus the capacitance of the sensor. Changes in capacitance are correlated with the concentration or presence of the target gas, enabling gas detection and quantification (Fig. 9b). Halide perovskites are used as the sensitive layer of the sensor, and their surfaces are usually modified with specific molecules or functional groups for adsorbing target gas molecules. This adsorption can change the fluorescence properties of perovskites, especially by quenching fluorescence. They may cause changes in the surface charge state or cause changes in the local electric field. These changes can affect the fluorescence intensity or emission spectrum of the perovskite. The presence and concentration of target gas molecules are detected by measuring the fluorescence signal of halide perovskite fluorescent gas sensors. This usually involves the use of optical detection techniques to analyze changes in fluorescence intensity. There is usually a quantitative relationship between the change in the fluorescence signal and the concentration of the target gas, allowing the sensor to monitor changes in gas concentration in real time. The interaction between gas molecules and halide perovskites leads to detectable and quantifiable changes in luminescence, and even color changes can be observed with the naked eye (Fig. 9c).

4.2 Halide perovskite-based sensor devices for NO_x detection

Nitrogen oxides can contribute to the formation of acid rain, photochemical smog, and other pollutants that pose threats to both the ecosystem and human health, potentially causing harm to the eyes and lungs.[62–67] Consequently, implementing gas sensors for the monitoring of trace amounts of NO_x becomes crucial as a preventative measure against these environmental hazards. Traditional NO sensing metal oxides typically exhibit higher concentration NO detection limits,[68–70] and some require high operating temperatures (>60 °C).[71] This may be a result of the weak interactions between the metallic elements and the nitrogen oxides.[72] Thus, the key to advancing NO_x sensing materials, characterized by low operating temperatures and heightened sensitivity, involves exploring new elements with enhanced binding strength to NO_x. Halide perovskites have attracted considerable interest in academic research because of their superior optical properties, high sensitivity, and low detection limits.
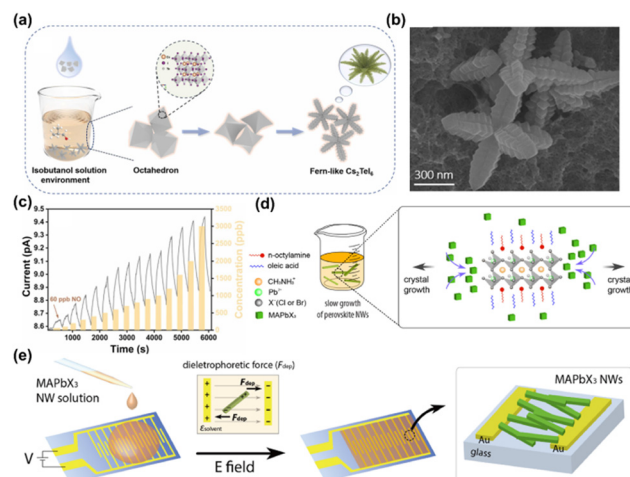

Fig. 10 (a) Synthesis process of fern-like Cs_2TeI_6 in isobutanol solution. (b) FESEM image of fern-like Cs_2TeI_6. (c) Real-time current values were observed as the NO concentration gradually increased (from 60 ppb to 3 ppm) at a constant voltage of 10 V.[73] Copyright 2022, Elsevier. (d) Schematic showing how $MAPbX_3$ (X = Cl or Br) grows from nanocube to NW. (e) Schematic representation of the alignment process on interdigitated electrode by dielectrophoresis.[74] Copyright 2021, Elsevier.

Inspired by Te–N orbital coordination, Lu *et al.* obtained Cs_2TeI_6 from the reaction of CsI and TeI_4.[73] The mixed powder of CsI and TeI_4 was dissolved in DMF/DMSO (molar ratio is 1:1) to prepare a precursor, and the precursor was quickly injected into isobutanol to obtain fern-like Cs_2TeI_6 crystals. The octahedral structure of Cs_2TeI_6 crystals forms a new shape due to phase collapse (Fig. 10a). The diameter of the fern-like Cs_2TeI_6 crystal was observed by FESEM to be approximately 700 nm (Fig. 10b). At room temperature, the synthesized Cs_2TeI_6 achieved a detection level of 60 ppb for NO in halide perovskites, which represents the lowest reported value for NO detection in halide perovskites. Furthermore, its high selectivity for NO and material stability demonstrates its excellent sensing performance. After NO comes into contact with the surface of Cs_2TeI_6, Te–N orbital coordination between NO and Cs_2TeI_6 gradually occurs, leading to an increase in current. When the supply of NO gas is stopped, the curve returns to near its original state (Fig. 10c). At 400 ppb NO concentration, the sensor response time under N_2 purge was 138 seconds, and the recovery time was 152 seconds. Choi *et al.* successfully synthesized single crystal MHP NWs through an improved reverse LARP method (Fig. 10d).[74] The authors introduced a DEP process on $MAPbCl_3$ and $MAPbBr_3$ NWs, in which the DEP force and torque were applied to the NWs in the fluid medium (*i.e.*, toluene), such that the MHP NWs were directionally deposited relative to the side, resulting in a consistent and controllable arrangement of the NWs (*i.e.*, self-arrangement). The relative equilibrium of hydrodynamic and DEP forces can describe the NW motion (Fig. 10e). The $MAPbBr_3$ NW sensor exhibits a consistent and substantial response to reductive gases such as H_2S (about 120%, 100 ppm) and NH_3

4442 | *Catal. Sci. Technol.*, 2024, **14**, 4432–4449

This journal is © The Royal Society of Chemistry 2024

(about 80%, 100 ppm) compared to oxidizing gases (*i.e.*, NO_2). Notably, positive changes in resistance were observed for both reductive and oxidative gases, indicating that carrier transport in the NW network is hindered by adsorption whenever target gas molecules are present. Their response is highly dependent on the dominant carrier type of the sensing material (n-type or p-type) and the properties of the gas analyte that donates or accepts electrons. The development of sensors to detect trace amounts of toxic gases is necessary. Yang *et al.* deposited a lead-free all-inorganic cesium copper iodide ($CsCu_2I_3$) perovskite as a gas-sensitive layer on a digital interelectrode pattern substrate through a simple spin-coating precursor.[75] The sensing performance of the perovskite $CsCu_2I_3$ nanostructured network sensor was measured at an excitation voltage of 20 mV. The sensor has superior room temperature NO_2 sensing performance, including an extremely low detection limit, excellent stable repeatability and selectivity. The resistance of the perovskite $CsCu_2I_3$ nanonetwork sensor decreases under the action of oxidizing gas NO_2, showing typical p-type behavior. The ultrasensitive NO_2 sensing performance of the $CsCu_2I_3$ nanostructure network is primarily due to its unique nanoneedle cluster network structure and abundant iodine vacancies on the perovskite surface. The sensor has great potential for indoor trace contaminant detection due to its high sensitivity and environmental friendliness.

Shi *et al.* fabricated a resistive gas sensor based on SCN ion-doped $CH_3NH_3PbI_3$ ($CH_3NH_3PbI_{3-x}(SCN)_x$, SCN-OHP).[76] By continuously spin-coating $Pb(SCN)_2$ and CH_3NH_3I solutions on the surface of a gold interdigital electrode, the SCN-OHP material can be deposited on the sensing layer (Fig. 11a). Varying the thickness of the sensor layer has a significant effect on how it performs. The thinner the prepared sensing layer, the greater its specific surface area and the number of gas molecules it can adsorb. The sensor

response (*R*) is the change in relative current at a bias voltage of 1 V: $R = \Delta I/I_0 = (I_{ex} - I_0)/I_0$, where I_0 and I_{ex} represent the pre- and post-exposure recordings of the target gas sensor, respectively. Fig. 11b shows the results of detecting 500 ppb NO_2. In the range of 0.5 to 5 ppm, the sensor signal exhibits linear growth with increasing nitrogen dioxide concentration. Chizhov *et al.* synthesized a composite material based on nanocrystalline ZnO and colloidal cubic perovskite $CsPbBr_3$ NCs.[77] The $CsPbBr_3$ nanocrystals were wrapped with oleic acid and oleylamine. When the detected NO_2 concentration is stabilized at 3 ppm and the humidity is raised from 1% to 100%, the sensor signal decreases by 38.5%, but the detected absolute value is still high (Fig. 11c). The $ZnO/CsPbBr_3$ nanocomposite sensors showed response to NO_2 in the concentration range of 0.5–3.0 ppm under cyclic light in the temperature range of 25–100 °C. The pure nanocrystalline ZnO sensor could only show a response to NO_2 above 100 °C under the same conditions. The photogenerated electron transfer from $CsPbBr_3$ NCs to ZnO has a high electron transfer rate constant, which ensures the effective separation of the photogenerated carriers. The interaction between photogenerated carriers and adsorbed gas molecules is responsible for the increased gas sensitivity of nanocomposites compared to pure nanocrystalline ZnO.

4.3 Halide perovskite-based sensor devices for VOCs detection

Volatile organic compounds are a class of carbon-containing organic pollutants, most of which have low boiling points and are easily evaporated at room temperature. Volatile organic compounds pose a serious threat to human health, not only due to potential risks but also because of their adverse environmental effects, both in the short and long term. As people become increasingly concerned about the risks to public health associated with exposure to these hazardous VOCs, the demand for precise detection of these compounds is skyrocketing. Halide perovskites have the advantages of high sensitivity, low detection limits, fast response times, selectivity, versatility, and potential cost-effectiveness. These qualities make them promising candidates for the detection of volatile organic pollutants in a variety of environmental, industrial, and healthcare applications.

Chen *et al.* fabricated a $CsPbBr_2I$ (CPBI) perovskite self-powered detection device, and Fig. 12a shows a cross-sectional SEM image of a typical CPBI device.[78] The photocurrent increases upon exposure to reducing gases (*e.g.*, acetone and propane) and oxidizing gases (*e.g.*, NO_2 and O_2). When reduced to an inert atmosphere, the photocurrent rapidly decreases. Under simulated sunlight, the CPBI device exhibited a linear response to both acetone and methanol over the test concentration ranging from 0 to 8 ppm, with a detection limit of 1 ppm for each (Fig. 12b). The authors proposed the chemical sensing mechanism of the CPBI detection device (Fig. 12c). Upon excitation by light, CPBI undergoes initial excitation, leading to rapid electron collection through the TiO_2 hole blocking layer on the FTO substrate, while the resulting
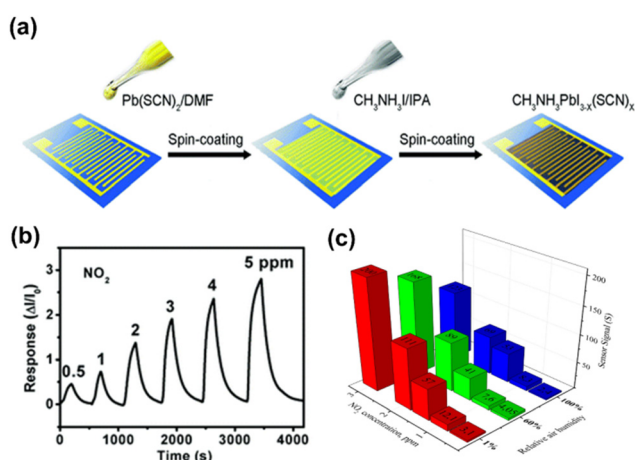
Fig. 11 (a) A schematic diagram of a gas sensor with a SCN-OHP sensing layer. (b) Response of sensor (120) when exposed to NO_2 concentrations ranging from 500 ppb to 5 ppm.[76] Copyright 2017, The Royal Society of Chemistry. (c) NO_2 sensing performance of ZnO/$CsPbBr_3$ nanocomposite at different relative humidities at 75 °C.[77] Copyright 2020, Elsevier.

This journal is © The Royal Society of Chemistry 2024

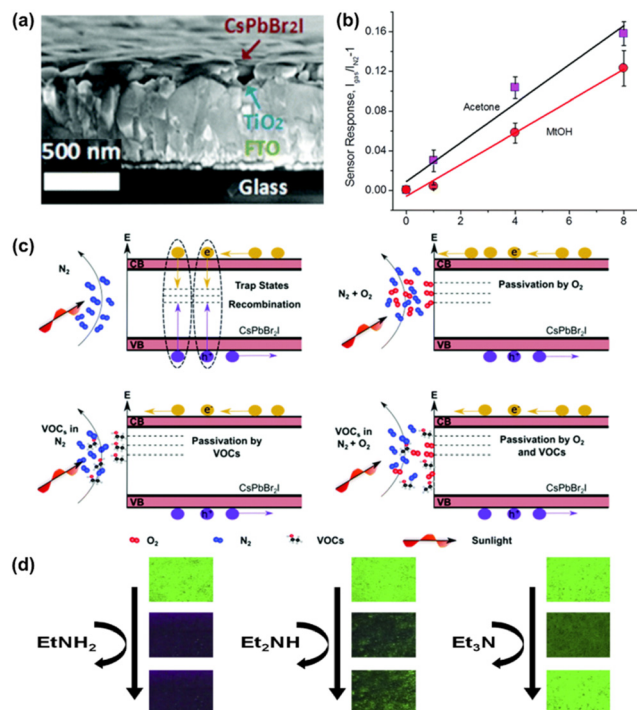*Catal. Sci. Technol.*, 2024, **14**, 4432–4449 | **4443**

Fig. 12 (a) Cross-sectional SEM image of a typical CPBI device. (b) The response of the CPBI sensor changes with the concentration of acetone and methanol in N_2. (c) CPBI chemical sensing mechanism schematic.[78] Copyright 2019, The Royal Society of Chemistry. (d) Photographs of blade-coated perovskite films recorded under 365 nm UV light after exposure to monoethylamine ($EtNH_2$), diethylamine (Et_2-NH), and trimethylamine (Et_3N).[61] Copyright 2017, Elsevier.

holes are directly transferred to the top Au contact. Only photogenerated charges other than the recombination of photogenerated electrons and holes can be effectively collected to form the measured photocurrent. In the N_2 atmosphere, the reason for the weak PL intensity is that the nonradiative recombination between photogenerated charges is stronger, resulting in a relatively small photocurrent in the output circuit. Photoluminescence (PL) spectra intensity and photocurrent are significantly increased in the presence of O_2. This may be attributed to the passivation of trap states by O_2 molecules. Kim *et al.* prepared a fluorescent chemical sensor based on organic–inorganic hybrid $CH_3NH_3PbBr_3$ perovskite nanoparticles, which can be used to detect VOCs and aliphatic amines, including monoethylamine, diethylamine, and trimethylamine.[61] The crystal structure of $CH_3NH_3PbBr_3$ is prone to structural changes, resulting in a burst of fluorescence signal when exposed to fatty amine gas. The detection of VOCs and fatty amine gas can be achieved by measuring their fluorescence intensity. After exposure to vapors of Et_3N and Et_2-NH_2, the intensity of the PL spectrum light decreased rapidly (<1 s) and dropped sharply to 1.0% of the initial light intensity. The color change of the material before and after exposure to gas is also visible to the naked eye (Fig. 12d). The exposure intensity of the $CH_3NH_3PbBr_3$ film can be recovered reversibly at different ratios and with different rates of recovery after complete exposure. The crystal structure of organometallic

halide perovskites can be disrupted by incorporating polar molecules (*e.g.*, H_2O) into the perovskite lattice, which can form hydrogen bonds with the halide. This causes the hydrogen bonds in the original perovskite structure to be broken. The authors conducted DFT calculations and found that the hydrogen bond distances between the protons in $EtNH_2$, Et_2-NH_2, and Et_3N and the nitrogen in CH_3NH^{3+} are 1.07, 2.25, and 3.58 Å, respectively. The findings indicate that increasing the distance between Et_3N and CH_3NH^{3+} weakens their interaction intensity, thereby enabling reversible fluorescence detection. However, the short distance between Et_3N and CH_3NH^{3+} leads to irreversible fluorescence detection behavior.

Takshi *et al.* studied the susceptibility and selectivity of methylammonium lead iodide ($MAPbI_3$) to methanol, ethanol, propanol, and isopropanol.[79] They first formed microchannels on indium tin oxide (ITO)-coated plastic substrates and then filled them with a solution of perovskite precursors by using capillary motion forces (Fig. 13a). The material has a more pronounced response to exposure to methanol vapors, with a percentage change in current exceeding 20% from +2.0 V to −2.0 V. Chen *et al.* deposited CsPbBr (CPB) on a fluorine-doped tin oxide layer to prepare the porous interconnection layer of the detector.[80] Electron microscopy analysis shows that there is a well-adhered and uniform CPB layer on the FTO surface, with an average thickness of 350 ± 5 nm (Fig. 13b). Fig. 13c shows the CPB sensor layout, morphology, structure, and optical properties. Under visible light irradiation, the material exhibits rapid sensing capability for acetone and ethanol at concentrations as low as 1 ppm in simulated atmospheres, with detection sensitivities of 0.03 and 0.025, respectively (Fig. 13d and e). The absolute value of the current is about 1.98 and 3.95 nA. The authors concluded that ethanol and acetone can serve as vacancy fillers to reversibly fill the inherent Br vacancies in CPB. The Br vacancies serve as traps for photogenerated charges, and when the device is subjected to the detection gas, the Br vacancy density decreases, allowing more photogenerated charges to be transported and thus an increase in photocurrent can be observed.
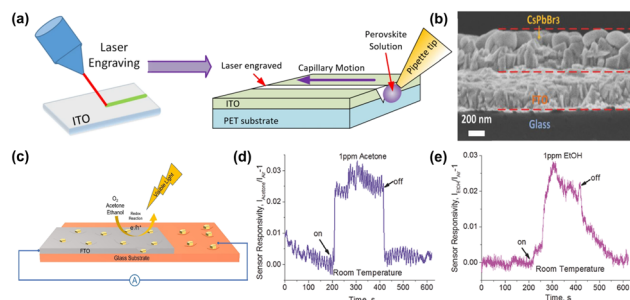

Fig. 13 (a) Schematic of the fabrication process for the gas sensor.[79] Copyright 2021, Springer Nature. (b) SEM image of cross section of CPB film. (c) Schematic representation of the morphology, structure, and optical characteristics of the CPB chemical sensor. Dynamic CPB sensor responsivity to injection of 1 ppm of (d) acetone and (e) ethanol in air at room temperature under visible-light irradiation.[80] Copyright 2017, Wiley-VCH Verlag.

4.4 Halide perovskite-based sensor devices for other gaseous pollutant detection

Halide perovskites have an abundance of surface-active sites that can chemically adsorb and react with various gas molecules, resulting in changes in the optoelectronic properties of the material, such as conductivity, light absorption, *etc.* These changes in performance can be monitored by photoelectric property testing or electrical testing, allowing gas detection and identification. The halide perovskite sensor is therefore capable of detecting NH_3 and H_2S at various concentration levels with a wide detection range, fast response and recovery time.

Ghosh *et al.* reported a material ($CH_3NH_3PbI_3$/MAPI) as a fast-responsive, selective, and sensitive active material for visual and electrical detection of ammonia (NH_3) gas.[81] The sensor is grown on commercially available cellulose paper and can selectively detect NH_3 gas at sub-ppm levels based on a visually visible color change (10 ppm) solution and highly sensitive electrical sensing. The sensor can also be used for visual and electrical sensing at room temperature. In the presence of a certain concentration of NH_3, the paper sensor made of $MAPbI_3$ and $FAPbI_3$ changed from black to yellow, while $MAPbBr_3$ changed from orange to white (Fig. 14a). Fig. 14b shows the current response of devices based on MAPB and FAPI at ambient temperatures with different NH_3 gas concentrations (ppm). The sensitivity (visual and electrical) diagrams of the three halide perovskites show that MAPI can perform visual detection and 10 ppb electrical detection at 10 ppm, MAPB can perform visual detection and 50 ppm electrical detection at 300 ppb, and for FAPI, the corresponding values are 80 ppm and 500 ppb, respectively (Fig. 14c). Saxena *et al.* synthesized ethylenediamine lead iodide chloride perovskite material.[82] The color of the perovskite film was observed to change from yellow to orange when the prepared material was exposed to ammonia vapor. When exposed to a lower concentration of ammonia (50–200 ppm), the perovskite film changes color from yellow to orange and returns to yellow within approximately 60 seconds. It is also possible to detect ammonia vapor at various ppm concentrations from 50 ppm to 200 ppm for a certain period of time by resistance measurement (Fig. 14d). At the lower concentration of 50 ppm, the response time is longer (39 seconds) with a resistance change of 1.37×10^{10} Ω, while at higher concentrations, the sensor responds faster, with a minimum response time of 16.5 seconds at 200 ppm, and the resistance change is 1.68×10^{10} Ω. Ammonia vapor infiltration into the perovskite film induces the release of free electrons within its structure, thereby increasing conductivity. Therefore, the resistance change increases with increasing concentration. After reaching a certain concentration, further exposure does not result in an additional increase in conductivity because there are no available sites or voids on the surface of the material, so the resistance change becomes saturated at higher concentrations. Ayesh *et al.* fabricated a gas sensor for detecting H_2S gas based on $FAPbBr_3$ material.[83] The material exhibits excellent optical luminescence, good charge transport, and high sensitivity to gas molecules. It exhibits high sensitivity to H_2S gas in the form of conductivity changes, and the adsorption of H_2S gas on the nanoparticles results in changes in their surface charge, thereby changing their conductivity. The sensor's response to H_2S gas shows high sensitivity to gas concentrations in the range of 0.5–100 ppm (Fig. 14e).

Conclusion

In recent years, many interesting studies on HP-based photocatalysts have been reported and highlighted. However, the application of HPs in photocatalytic removal of gaseous pollutants remains in its nascent stages. Their overall performance and stability are currently unsatisfactory, limiting their efficiency in addressing energy and environmental issues, and facing several challenges. Halide perovskite gas sensors have attracted widespread attention due to their high sensitivity, high selectivity, and low cost. Despite the excellent performance of these sensors, several aspects of their practical applications require further exploration. This review clarified the mechanism of photocatalytic reaction and gas detection of halide perovskites. The materials were briefly classified, and the research on the photocatalytic removal of NO_x and VOCs and the detection of these pollutant gases were described.

Looking ahead, the research on halide perovskites presents both limitless opportunities and challenges. This field remains in the exploratory stage. Beyond the research content introduced in this review, halide perovskites also exhibit emerging development trends and challenges in other aspects:

(i) Halide perovskites are not only effective in the photocatalytic degradation of gaseous pollutants but also show promise in degrading organic dyes, organic wastes in wastewater, drug residues, and other pollutants. They can be utilized in industrial wastewater treatment and environmental restoration.
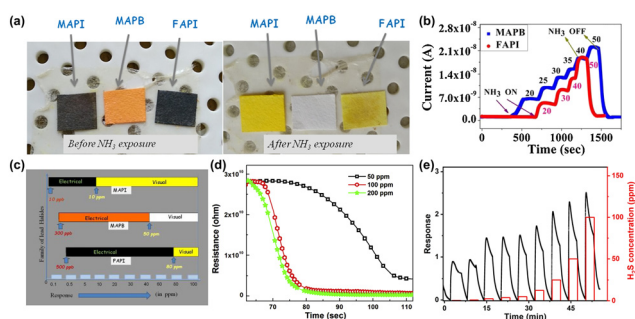

Fig. 14 (a) Photographs of MAPI, MAPB, and FAPI films before NH_3 gas exposure (pristine films) and after NH_3 gas exposure. (b) The current response of MAPB and FAPI paper-based sensors at different NH_3 gas concentrations (ppm). (c) Schematic representation of the MAPI, MAPB, and FAPI sensitivity scales.[81] Copyright 2020, Elsevier. (d) Resistance *versus* time curve for different concentrations of ammonia vapor.[82] Copyright 2018, Elsevier. (e) Sensor gas response at different gas concentrations while the sensor is inside a Teflon chamber and room light is on.[83] Copyright 2022, Elsevier.

This journal is © The Royal Society of Chemistry 2024

Catal. Sci. Technol., 2024, **14**, 4432–4449 | **4445**

(ii) Halide perovskites can be applied to photocatalytic water splitting to produce hydrogen, thereby contributing to sustainable hydrogen energy production, reducing dependence on fossil fuels, and lowering greenhouse gas emissions. Additionally, their photocatalytic activity can inhibit bacterial growth, providing an antibacterial effect that enhances water and air quality.

(iii) The application of halide perovskite sensors extends from industrial settings to environmental monitoring. These sensors, characterized by their small size, light weight, and low power consumption, can be developed into portable or embedded gas monitoring devices for outdoor activities, indoor air quality testing, and industrial safety testing. They enable continuous gas monitoring and can be integrated into intelligent monitoring systems for real-time monitoring and data collection of urban air quality, thus providing a scientific basis for urban planning, traffic management, and environmental protection.

(iv) Organic halide perovskites have poor stability under humid conditions and high temperatures, which are susceptible to dissociation or loss of crystallinity in moisture, resulting in a decline in material performance. Therefore, limiting their use in environments such as solar cells where they are exposed to sunlight for long periods. Furthermore, the challenges in large-area preparation and scaling also limited their practical application. When preparing large-area films, it becomes more difficult to control the structure and quality of the crystals, often leading to crystal defects. This affects the long-term stability and reliability of the device. Achieving efficient halide perovskites usually requires strict process controls and conditions, which increases costs and introduces uncertainty into material production.

Regarding the practical application of halide perovskites, we believe that more and more scholars will devote themselves to solving the current problems, thus promoting the halide perovskites from laboratory research to industrialization.

Data availability

No primary research results, software or code have been included and no new data were generated or analysed as part of this review.

Conflicts of interest

There are no conflicts to declare.

Acknowledgements

References

1 X. Qian, Y. Ma, X. Xia, J. Xia, J. Ye, G. He and H. Chen, Recent progress on $Bi_4O_5Br_2$-based photocatalysts for environmental remediation and energy conversion, *Catal. Sci. Technol.*, 2023, **14**, 1085–1104.

2 J. Wang, J. Xuan, X. Wei, Y. Zhang, J. Fan, L. Ni, Y. Yang, J. Liu, Y. Tian and X. Wang, Enhancing solar-to-hydrogen efficiency with an S-scheme $GaTe/PtS_2$ van der Waals heterojunction with high light absorption, *Catal. Sci. Technol.*, 2023, **13**, 4753–4764.

3 A. Ghosh, D. Nag, R. Chatterjee, A. Singha, P. S. Dash, B. Choudhury and A. Bhaumik, CO_2 to dimethyl ether (DME): structural and functional insights of hybrid catalysts, *Catal. Sci. Technol.*, 2024, **14**, 1387–1427.

4 G. Zhu, J. Zhou, D. Li and Z. Ao, Density functional theory study on the enhanced adsorption mechanism of VOCs by Cu_4 cluster decorated UiO-66, *Surf. Interfaces*, 2024, **46**, 104199.

5 N. Joshi, P. Gawas, A. Bora, L. Sivachandiran, Y. Sivalingam and V. Nutalapati, Effect of thermal treatment on zeolite for real-time gas sensing of oxygenated volatile organic compounds, *Surf. Interfaces*, 2023, **42**, 103364.

6 R. Li, Y. Rao and Y. Huang, Advances in catalytic elimination of atmospheric pollutants by two-dimensional transition metal oxides, *Chin. Chem. Lett.*, 2023, **34**, 108000.

7 J. Wang, X. Tang, J. Li, S. Dong, X. Zhang and B. Liu, Fabrication of high-performance $CeO_2–MnO_x/TiO_2/Ti$ monolithic catalysts for low-temperature and stable CO oxidation, *Catal. Sci. Technol.*, 2023, **13**, 3386–3394.

8 X. Li, P. Wang, S. Han, Y. Huang, W. Ho, S. S. H. Ho, S.-C. Lee and M. Wang, Development and application of photocatalytic coating for roadside NO_x mitigation in Hong Kong, *Chin. Chem. Lett.*, 2024, **35**, 108709.

9 D. Song, M. Li, F. Yang, M. Yu, Z. Li, J. Chen, X. Zhang and W. Zhou, Plasmon Bi in-situ anchored on BiOCl nanosheets assembled microspheres towards optimized photothermal-photocatalytic performance, *Chin. Chem. Lett.*, 2024, **35**, 108591.

10 H. Liu, S. Hussain, S. H. A. Jaffery, J. Lee, S. Aftab, J. Jung, H.-S. Kim, J. Kang and D. Vikraman, Construction of perovskite solar cells and X-ray detectors using the indium selenide-carbon nanotube hybrids tuned hole transporting layer, *Surf. Interfaces*, 2023, **41**, 103234.

11 G. Xing, N. Mathews, S. Sun, S. S. Lim, Y. M. Lam, M. Grätzel, S. Mhaisalkar and T. C. Sum, Long-range balanced electron-and hole-transport lengths in organic-inorganic $CH_3NH_3PbI_3$, *Science*, 2013, **342**, 344–347.

12 Q. Dong, Y. Fang, Y. Shao, P. Mulligan, J. Qiu, L. Cao and J. Huang, Electron-hole diffusion lengths > 175 μm in solution-grown $CH_3NH_3PbI_3$ single crystals, *Science*, 2015, **347**, 967–970.

13 L. Wang, H. Wang, M. Wagner, Y. Yan, D. S. Jakob and X. G. Xu, Nanoscale simultaneous chemical and mechanical imaging via peak force infrared microscopy, *Sci. Adv.*, 2017, **3**, e1700255.

4446 | *Catal. Sci. Technol.*, 2024, **14**, 4432–4449

This journal is © The Royal Society of Chemistry 2024

14 Y. Yang, Y. Yan, M. Yang, S. Choi, K. Zhu, J. M. Luther and M. C. Beard, Low surface recombination velocity in solution-grown $CH_3NH_3PbBr_3$ perovskite single crystal, *Nat. Commun.*, 2015, **6**, 7961.

15 S. Li, D. Lei, W. Ren, X. Guo, S. Wu, Y. Zhu, A. L. Rogach, M. Chhowalla and A. K.-Y. Jen, Water-resistant perovskite nanodots enable robust two-photon lasing in aqueous environment, *Nat. Commun.*, 2020, **11**, 1192.

16 F. Liu, Y. Zhang, C. Ding, S. Kobayashi, T. Izuishi, N. Nakazawa, T. Toyoda, T. Ohta, S. Hayase and T. Minemoto, Highly luminescent phase-stable $CsPbI_3$ perovskite quantum dots achieving near 100% absolute photoluminescence quantum yield, *ACS Nano*, 2017, **11**, 10373–10383.

17 Y.-H. Kim, H. Cho and T.-W. Lee, Metal halide perovskite light emitters, *Proc. Natl. Acad. Sci. U. S. A.*, 2016, **113**, 11694–11702.

18 F. Hu, H. Zhang, C. Sun, C. Yin, B. Lv, C. Zhang, W. W. Yu, X. Wang, Y. Zhang and M. Xiao, Superior optical properties of perovskite nanocrystals as single photon emitters, *ACS Nano*, 2015, **9**, 12410–12416.

19 A. A. Qureshi, S. Javed, A. Fakharuddin, M. A. Akram and L. Schmidt-Mende, Low-temperature processed natural hematite as an electron extraction layer for efficient and stable perovskite solar cells, *Surf. Interfaces*, 2023, **40**, 103003.

20 N. T. Shelke, M. Yewale, R. Kadam, U. Nakate, A. Jadhavar and D. Shin, Facile hydrothermal synthesis and fabrication of nickel cobalt oxide as an advanced electrode for electrochemical capacitors, *Surf. Interfaces*, 2023, **43**, 103555.

21 E. Gagaoudakis, A. Panagiotopoulos, T. Maksudov, M. Moschogiannaki, D. Katerinopoulou, G. Kakavelakis, G. Kiriakidis, V. Binas, E. Kymakis and K. Petridis, Self-powered, flexible and room temperature operated solution processed hybrid metal halide p-type sensing element for efficient hydrogen detection, *JPhys Mater.*, 2020, **3**, 014010.

22 M.-Y. Zhu, L.-X. Zhang, J. Yin, J.-J. Chen, L.-J. Bie and B. D. Fahlman, Physisorption induced p-xylene gas-sensing performance of $(C_4H_9NH_3)_2PbI_4$ layered perovskite, *Sens. Actuators, B*, 2019, **282**, 659–664.

23 W. Jiao, J. He and L. Zhang, Synthesis and high ammonia gas sensitivity of (CH_3NH_3) $PbBr_{3-x}I_x$ perovskite thin film at room temperature, *Sens. Actuators, B*, 2020, **309**, 127786.

24 L. Chu, W. Ahmad, W. Liu, J. Yang, R. Zhang, Y. Sun, J. Yang and X. A. Li, Lead-free halide double perovskite materials: a new superstar toward green and stable optoelectronic applications, *Nanomicro Lett.*, 2019, **11**, 1–18.

25 M. Saliba, T. Matsui, J.-Y. Seo, K. Domanski, J.-P. Correa-Baena, M. K. Nazeeruddin, S. M. Zakeeruddin, W. Tress, A. Abate and A. Hagfeldt, Cesium-containing triple cation perovskite solar cells: improved stability, reproducibility and high efficiency, *Energy Environ. Sci.*, 2016, **9**, 1989–1997.

26 Z. Xiao, K.-Z. Du, W. Meng, J. Wang, D. B. Mitzi and Y. Yan, Intrinsic Instability of $Cs_2In(I)M(III)X_6$ (M = Bi, Sb; X = Halogen) Double Perovskites: A Combined Density Functional Theory and Experimental Study, *J. Am. Chem. Soc.*, 2017, **139**, 6054–6057.

27 C. Pi, W. Chen, W. Zhou, S. Yan, Z. Liu, C. Wang, Q. Guo, J. Qiu, X. Yu and B. Liu, Highly stable humidity sensor based on lead-free $Cs_3Bi_2Br_9$ perovskite for breath monitoring, *J. Mater. Chem. C*, 2021, **9**, 11299–11305.

28 W.-J. Yin, Y. Yan and S.-H. Wei, Anomalous Alloy Properties in Mixed Halide Perovskites, *J. Phys. Chem. Lett.*, 2014, **5**, 3625–3631.

29 M. G. Walter, E. L. Warren, J. R. McKone, S. W. Boettcher, Q. Mi, E. A. Santori and N. S. Lewis, Solar water splitting cells, *Chem. Rev.*, 2010, **110**, 6446–6473.

30 M. A. Henderson, A surface science perspective on TiO_2 photocatalysis, *Surf. Sci. Rep.*, 2011, **66**, 185–297.

31 H. Huang, M. I. Bodnarchuk, S. V. Kershaw, M. V. Kovalenko and A. L. Rogach, Lead halide perovskite nanocrystals in the research spotlight: stability and defect tolerance, *ACS Energy Lett.*, 2017, **2**, 2071–2083.

32 G. Gao, Q. Xi, H. Zhou, Y. Zhao, C. Wu, L. Wang, P. Guo and J. Xu, Novel inorganic perovskite quantum dots for photocatalysis, *Nanoscale*, 2017, **9**, 12032–12038.

33 J. Yang, X. Wang, H. Wang, F. Dong and M. Zhu, $CsPbBr_3$ perovskite nanocrystal: A robust photocatalyst for realizing NO abatement, *ACS ES&T Eng.*, 2021, **1**, 1021–1027.

34 D. Wu, Y. Tao, Y. Huang, B. Huo, X. Zhao, J. Yang, X. Jiang, Q. Huang, F. Dong and X. Tang, High visible-light photocatalytic performance of stable lead-free $Cs_2AgBiBr_6$ double perovskite nanocrystals, *J. Catal.*, 2021, **397**, 27–35.

35 J. Kou, C. Lu, J. Wang, Y. Chen, Z. Xu and R. S. Varma, Selectivity enhancement in heterogeneous photocatalytic transformations, *Chem. Rev.*, 2017, **117**, 1445–1514.

36 J. Yang, B. Liu, L. Zeng, B. Du, Y. Zhou, H. Tao, Y. Yun and M. Zhu, Confining Bismuth-Halide Perovskite in Mesochannels of Silica Nanomembranes for Exceptional Photocatalytic Abatement of Air Pollutants, *Angew. Chem., Int. Ed.*, 2024, e202319741.

37 B. Huo, J. Yang, Y. Bian, D. Wu, J. Feng, J. Zhou, Q. Huang, F. Dong and X. Tang, Amino-mediated anchoring of $FAPbBr_3$ perovskite quantum dots on silica spheres for efficient visible light photocatalytic NO removal, *Chem. Eng. J.*, 2021, **406**, 126740.

38 Z. Guan, Y. Wu, P. Wang, Q. Zhang, Z. Wang, Z. Zheng, Y. Liu, Y. Dai, M.-H. Whangbo and B. Huang, Perovskite photocatalyst $CsPbBr_{3-x}I_x$ with a bandgap funnel structure for H_2 evolution under visible light, *Appl. Catal., B*, 2019, **245**, 522–527.

39 Q. Xu, L. Zhang, B. Cheng, J. Fan and J. Yu, S-scheme heterojunction photocatalyst, *Chem*, 2020, **6**, 1543–1559.

40 G. Zhang, C. Yuan, X. Li, L. Yang, W. Yang, R. Fang, Y. Sun, J. Sheng and F. Dong, The mechanisms of interfacial charge transfer and photocatalysis reaction over $Cs_3Bi_2Cl_9$ QD/$(BiO)_2CO_3$ heterojunction, *Chem. Eng. J.*, 2022, **430**, 132974.

41 T. Tan, X. Wang, X. Zhou, H. Ma, R. Fang, Q. Geng and F. Dong, Highly active Cs_2SnCl_6/C_3N_4 heterojunction photocatalysts operating via interfacial charge transfer mechanism, *J. Hazard. Mater.*, 2022, **439**, 129694.

42 F. Zhong, C. Yuan, Y. He, Y. Sun, J. Sheng and F. Dong, Dual-quantum-dots heterostructure with confined active

This journal is © The Royal Society of Chemistry 2024

Catal. Sci. Technol., 2024, **14**, 4432–4449 | **4447**

interface for promoted photocatalytic NO abatement, *J. Hazard. Mater.*, 2022, **438**, 129463.

43 B. Xie, D. Chen, N. Li, Q. Xu, H. Li, J. He and J. Lu, Fabrication of an FAPbBr$_3$/g-C$_3$N$_4$ heterojunction to enhance NO removal efficiency under visible-light irradiation, *Chem. Eng. J.*, 2022, **430**, 132968.

44 Y. Zhang, W. Yu, S. Cao, Z. Sun, X. Nie, Y. Liu and Z. Zhao, Photocatalytic chemoselective transfer hydrogenation of quinolines to tetrahydroquinolines on hierarchical NiO/In$_2$O$_3$–CdS microspheres, *ACS Catal.*, 2021, **11**, 13408–13415.

45 W. Weng, S. Wang, W. Xiao and X. W. Lou, Direct conversion of rice husks to nanostructured SiC/C for CO$_2$ photoreduction, *Adv. Mater.*, 2020, **32**, 2001560.

46 D. Cardenas-Morcoso, A. S. F. Gualdrón-Reyes, A. B. Ferreira Vitoreti, M. García-Tecedor, S. J. Yoon, M. Solis de la Fuente, I. N. Mora-Seró and S. Gimenez, Photocatalytic and photoelectrochemical degradation of organic compounds with all-inorganic metal halide perovskite quantum dots, *J. Phys. Chem. Lett.*, 2019, **10**, 630–636.

47 D. Wu, W. Sang, B. Huo, J. Wang, X. Wang, C. Chen, Q. Huang and X. Tang, Highly crystalline lead-free Cs$_3$Sb$_2$Br$_9$ perovskite microcrystals enable efficient and selective photocatalytic oxidation of benzyl alcohol, *J. Catal.*, 2022, **408**, 36–42.

48 B. Bajorowicz, A. Mikolajczyk, H. P. Pinto, M. Miodynska, W. Lisowski, T. Klimczuk, I. Kaplan-Ashiri, M. Kazes, D. Oron and A. Zaleska-Medynska, Integrated experimental and theoretical approach for efficient design and synthesis of gold-based double halide perovskites, *J. Phys. Chem. C*, 2020, **124**, 26769–26779.

49 Z.-J. Bai, X.-P. Tan, L. Chen, B. Hu, Y.-X. Tan, Y. Mao, S. Shen, J.-K. Guo, C.-T. Au and Z.-W. Liang, Efficient photocatalytic toluene selective oxidation over Cs$_3$Bi$_{1.8}$Sb$_{0.2}$Br$_9$ Nanosheets: Enhanced charge carriers generation and C–H bond dissociation, *Chem. Eng. Sci.*, 2022, **247**, 116983.

50 Y. Dai, C. Poidevin, C. Ochoa-Hernández, A. A. Auer and H. Tüysüz, A supported bismuth halide perovskite photocatalyst for selective aliphatic and aromatic C–H bond activation, *Angew. Chem.*, 2020, **132**, 5837–5845.

51 P. Qiu, Q. Wang, Y. Zhao, Y. Dai, Y. Dong, C. Chen, Q. Chen and Y. Li, Fabricating surface-functionalized CsPbBr$_3$/Cs$_4$-PbBr$_6$ nanosheets for visible-light photocatalytic oxidation of styrene, *Front. Chem.*, 2020, **8**, 130.

52 H. Huang, H. Yuan, K. P. Janssen, G. Solis-Fernandez, Y. Wang, C. Y. Tan, D. Jonckheere, E. Debroye, J. Long and J. Hendrix, Efficient and selective photocatalytic oxidation of benzylic alcohols with hybrid organic–inorganic perovskite materials, *ACS Energy Lett.*, 2018, **3**, 755–759.

53 Q. Li, T. Song, Y. Zhang, Q. Wang and Y. Yang, Boosting Photocatalytic Activity and Stability of Lead-Free Cs$_3$Bi$_2$Br$_9$ Perovskite Nanocrystals via In Situ Growth on Monolayer 2D Ti$_3$C$_2$Tx MXene for C–H Bond Oxidation, *ACS Appl. Mater. Interfaces*, 2021, **13**, 27323–27333.

54 M. Zhang, W. Wang, F. Gao and D. Luo, g-C$_3$N$_4$-Stabilised Organic–Inorganic Halide Perovskites for Efficient Photocatalytic Selective Oxidation of Benzyl Alcohol, *Catalysts*, 2021, **11**, 505.

55 Z.-J. Bai, Y. Mao, B.-H. Wang, L. Chen, S. Tian, B. Hu, Y.-J. Li, C.-T. Au and S.-F. Yin, Tuning photocatalytic performance of Cs$_3$Bi$_2$Br$_9$ perovskite by g-C$_3$N$_4$ for C (sp^3)—H bond activation, *Nano Res.*, 2023, **16**, 6104–6112.

56 A. Ummadisingu, L. Steier, J.-Y. Seo, T. Matsui, A. Abate, W. Tress and M. Grätzel, The effect of illumination on the formation of metal halide perovskite films, *Nature*, 2017, **545**, 208–212.

57 Y. Lou, M. Fang, J. Chen and Y. Zhao, Formation of highly luminescent cesium bismuth halide perovskite quantum dots tuned by anion exchange, *Chem. Commun.*, 2018, **54**, 3779–3782.

58 Y. Yang, Z. Chen, H. Huang, Y. Liu, J. Zou, S. Shen, J. Yan, J. Zhang, Z. Zhuang and Z. Luo, Synergistic surface activation during photocatalysis on perovskite derivative sites in heterojunction, *Appl. Catal., B*, 2023, **323**, 122146.

59 S. Zampolli, I. Elmi, F. Ahmed, M. Passini, G. Cardinali, S. Nicoletti and L. Dori, An electronic nose based on solid state sensor arrays for low-cost indoor air quality monitoring applications, *Sens. Actuators, B*, 2004, **101**, 39–46.

60 X. L. Yu, Y. Wang, Y. M. Hu, C. B. Cao and H. L. W. Chan, Gas-Sensing Properties of Perovskite BiFeO$_3$ Nanoparticles, *J. Am. Ceram. Soc.*, 2009, **92**, 3105–3107.

61 S.-H. Kim, A. Kirakosyan, J. Choi and J. H. Kim, Detection of volatile organic compounds (VOCs), aliphatic amines, using highly fluorescent organic-inorganic hybrid perovskite nanoparticles, *Dyes Pigm.*, 2017, **147**, 1–5.

62 C.-Y. Lin, J.-G. Chen, C.-W. Hu, J. J. Tunney and K.-C. Ho, Using a PEDOT: PSS modified electrode for detecting nitric oxide gas, *Sens. Actuators, B*, 2009, **140**, 402–406.

63 H. Jin, Y. Huang and J. Jian, Plate-like Cr$_2$O$_3$ for highly selective sensing of nitric oxide, *Sens. Actuators, B*, 2015, **206**, 107–110.

64 J. Qiu, X. Hu, X. Min, W. Quan, R. Tian, P. Ji, H. Zheng, W. Qin, H. Wang and T. Pan, Observation of switchable dual-conductive channels and related nitric oxide gas-sensing properties in the N-rGO/ZnO heterogeneous structure, *ACS Appl. Mater. Interfaces*, 2020, **12**, 19755–19767.

65 B. Peng, Y. Zhou, G. Liu, Y. He, C. Gao and Y. Guo, An ultra-sensitive detection system for sulfur dioxide and nitric oxide based on improved differential optical absorption spectroscopy method, *Spectrochim. Acta, Part A*, 2020, **233**, 118169.

66 W. Tsujita, A. Yoshino, H. Ishida and T. Moriizumi, Gas sensor network for air-pollution monitoring, *Sens. Actuators, B*, 2005, **110**, 304–311.

67 J.-Y. Jeon, B.-C. Kang, Y. T. Byun and T.-J. Ha, High-performance gas sensors based on single-wall carbon nanotube random networks for the detection of nitric oxide down to the ppb-level, *Nanoscale*, 2019, **11**, 1587–1594.

68 D. Degler, Trends and advances in the characterization of gas sensing materials based on semiconducting oxides, *Sensors*, 2018, **18**, 3544.

4448 | *Catal. Sci. Technol.*, 2024, **14**, 4432–4449

This journal is © The Royal Society of Chemistry 2024

69 J. Casanova-Cháfer, E. Navarrete, X. Noirfalise, P. Umek, C. Bittencourt and E. Llobet, Gas sensing with iridium oxide nanoparticle decorated carbon nanotubes, *Sensors*, 2018, **19**, 113.

70 Q. Wu, W. Liu, X. Bu, H. Wu, C. Wang, X. Li and X. Wang, Graphene oxide/graphene hybrid film with ultrahigh ammonia sensing performance, *Nanotechnology*, 2020, **32**, 115501.

71 N. D. Chinh, N. D. Quang, H. Lee, T. Thi Hien, N. M. Hieu, D. Kim, C. Kim and D. Kim, NO gas sensing kinetics at room temperature under UV light irradiation of In_2O_3 nanostructures, *Sci. Rep.*, 2016, **6**, 35066.

72 S. Hou, R. Pang, S. Chang, L. Ye, J. Xu, X. Wang, Y. Zhang, Y. Shang and A. Cao, Synergistic $CNFs/CoS_2/MoS_2$ flexible films with unprecedented selectivity for NO gas at room temperature, *ACS Appl. Mater. Interfaces*, 2020, **12**, 29778–29786.

73 Z.-K. Chen, W. Ye, J. Wang, C. Yu, J.-H. He and J.-M. Lu, Sensitive NO detection by lead-free halide Cs_2TeI_6 perovskite with Te-N bonding, *Sens. Actuators, B*, 2022, **357**, 131397.

74 A. Kirakosyan, M. R. Sihn, M.-G. Jeon, R. M. Kabir and J. Choi, Self-aligned $CH_3NH_3PbBr_3$ perovskite nanowires via dielectrophoresis for gas sensing applications, *Appl. Mater. Today*, 2022, **26**, 101307.

75 X. Sun, J. Yang, Z. Wu, G. Meng, X. Guo, D. Kuang, L. Xiong, W. Qu, X. Fang and X. Yang, Lead-free $CsCu_2I_3$ perovskite nanostructured networks gas sensor for selective detection of trace nitrogen dioxide at room temperature, *IEEE Sens. J.*, 2021, **21**, 14677–14684.

76 Y. Zhuang, W. Yuan, L. Qian, S. Chen and G. Shi, High-performance gas sensors based on a thiocyanate ion-doped organometal halide perovskite, *Phys. Chem. Chem. Phys.*, 2017, **19**, 12876–12881.

77 A. Chizhov, M. Rumyantseva, K. Drozdov, I. Krylov, M. Batuk, J. Hadermann, D. Filatova, N. Khmelevsky, V. Kozlovsky and L. Maltseva, Photoresistive gas sensor based on nanocrystalline ZnO sensitized with colloidal perovskite $CsPbBr_3$ nanocrystals, *Sens. Actuators, B*, 2021, **329**, 129035.

78 H. Chen, M. Zhang, X. Fu, Z. Fusco, R. Bo, B. Xing, H. T. Nguyen, C. Barugkin, J. Zheng and C. F. J. Lau, Light-activated inorganic $CsPbBr_2I$ perovskite for room-temperature self-powered chemical sensing, *Phys. Chem. Chem. Phys.*, 2019, **21**, 24187–24193.

79 M. Hossain and A. Takshi, Perovskite-based sensing scheme for detecting volatile organic compounds (VOCs) at room temperature, *MRS Adv.*, 2021, **6**, 645–649.

80 H. Chen, M. Zhang, R. Bo, C. Barugkin, J. Zheng, Q. Ma, S. Huang, A. W. Ho-Baillie, K. R. Catchpole and A. Tricoli, Superior self-powered room-temperature chemical sensing with light-activated inorganic halides perovskites, *Small*, 2018, **14**, 1702571.

81 A. Maity, S. Mitra, C. Das, S. Siraj, A. Raychaudhuri and B. Ghosh, Universal sensing of ammonia gas by family of lead halide perovskites based on paper sensors: Experiment and molecular dynamics, *Mater. Res. Bull.*, 2021, **136**, 111142.

82 N. Gupta, O. Nanda, R. Grover and K. Saxena, A new inorganic-organic hybrid halide perovskite thin film based ammonia sensor, *Org. Electron.*, 2018, **58**, 202–206.

83 A. I. Ayesh, S. Alghamdi, B. Salah, S. Bennett, C. Crean and P. J. Sellin, High sensitivity H_2S gas sensors using lead halide perovskite nanoparticles, *Results Phys.*, 2022, **35**, 105333.

This journal is © The Royal Society of Chemistry 2024

Catal. Sci. Technol., 2024, **14**, 4432–4449 | **4449**